AGU PUBLICATIONS

JGR

Journal of Geophysical Research: Oceans

RESEARCH ARTICLE

10.1002/2014JC010076

Key Points:
- SICC is composed of three eastward jets: sSICC, cSICC, and nSICC
- SICC jets seem to be related to PV staircase formation
- SICC has an associated thermal front at thermocline depths

Supporting Information:
- Readme
- Figures S1–S3

Correspondence to:
V. V. Menezes,
vivianev@utas.edu.au

Citation:
Menezes, V. V., H. E. Phillips, A. Schiller, N. L. Bindoff, C. M. Domingues, and M. L. Vianna (2014), South Indian Countercurrent and associated fronts, *J. Geophys. Res. Oceans*, *119*, 6763–6791, doi:10.1002/2014JC010076.

Received 20 APR 2014
Accepted 9 SEP 2014
Accepted article online 15 SEP 2014
Published online 15 OCT 2014

South Indian Countercurrent and associated fronts

Viviane V. Menezes[1,2,3], Helen E. Phillips[2,3], Andreas Schiller[4], Nathaniel L. Bindoff[2,3,4,5], Catia M. Domingues[2,5], and Marcio L. Vianna[6]

[1]CSIRO/UTAS Quantitative Marine Science PhD Program, Hobart, Tasmania, Australia, [2]Institute for Marine and Antarctic Studies, University of Tasmania, Hobart, Tasmania, Australia, [3]ARC Centre of Excellence in Climate System Science, Hobart, Tasmania, Australia, [4]Centre for Australian Weather and Climate Research and CSIRO Wealth from Oceans Flagship, Hobart, Tasmania, Australia, [5]Antarctic Climate and Ecosystems Cooperative Research Centre, Hobart, Tasmania, Australia, [6]VM Oceanica Ltd, São José dos Campos, Sao Paulo, Brazil

Abstract A striking feature of the South Indian Ocean circulation is the presence of the eastward South Indian Countercurrent (SICC) that flows in a direction opposite to that predicted by the classical theories of wind-driven circulation. Several authors suggest that the SICC resembles the subtropical countercurrents (STCCs) observed in other oceans, which are defined as narrow eastward jets on the equatorward side of subtropical gyres, where the depth-integrated flow is westward. These jets are associated with subsurface thermal fronts at thermocline depths by the thermal wind relation. However, the subsurface thermal front associated with the SICC has not been described to date. Other studies conjecture an important role for salinity in controlling the SICC. In the present work, we analyze three Argo-based atlases and data from six hydrographic cruises to investigate whether the SICC is accompanied by permanent thermal and density fronts including salinity effects. The seasonal cycle of these fronts in relation to the SICC strength is also investigated. We find that the SICC is better described as composed of three distinct jets, which we name the northern, central, and southern SICC. We find that the southern SICC around 26°S has an associated thermal front at subsurface depths around 100–200 m with salinity being of secondary importance. The southern branch strength is related to mode waters poleward of the front, similar to a STCC-like current. However, the SICC multiple jet structure seems to be better described as resulting from PV staircases.

1. Introduction

The upper ocean circulation of the South Indian Ocean (SIO) between 22°S and 30°S is characterized by the presence of the South Indian Countercurrent (SICC) [*Siedler et al*., 2006; *Palastanga et al*., 2007; *Schott et al*., 2009], a permanent eastward current that flows in a direction opposite to that predicted by classical theories of wind-driven circulation (Figure 1).

The SICC originates at the southern tip of Madagascar around 25°S, possibly fed by a partial retroflection of the East Madagascar Current [*Siedler et al*., 2006; *Palastanga et al*., 2007], and flows all the way across the basin from Madagascar to the west of Australia. In the eastern basin, the SICC seems to connect with the tropical eastward Eastern Gyral Current (EGC) around 15°S and with the Leeuwin Current, the only poleward-flowing eastern boundary current in the world [*Schott et al*., 2009, and references therein].

Although the SICC has only recently been recognized as a permanent feature of the SIO circulation, *Sharma* [1976] and *Sharma et al.* [1978] described a shallow eastward current between 22°S and 26°S associated with a thermal front. He named that current the South Indian Tropical Countercurrent, pointing out that it was evident in all surface geopotential charts from the Indian Ocean Atlas produced by Wyrtki in 1971 and also on the surface currents maps from the Royal Netherlands Meteorological Institute in 1952.

Despite being a permanent feature of the large-scale circulation, the formation mechanism and dynamics controlling the SICC are still largely unknown [*Palastanga et al*., 2007; *Siedler et al*., 2006; *Schott et al*., 2009]. Since the SICC flows opposite to the direction predicted by classical theories of wind-driven circulation, and its geographic location is at the same latitude range as the subtropical countercurrents (STCC) observed in the Pacific and North Atlantic, many authors [e.g., *Sharma*, 1976; *Siedler et al*., 2006;

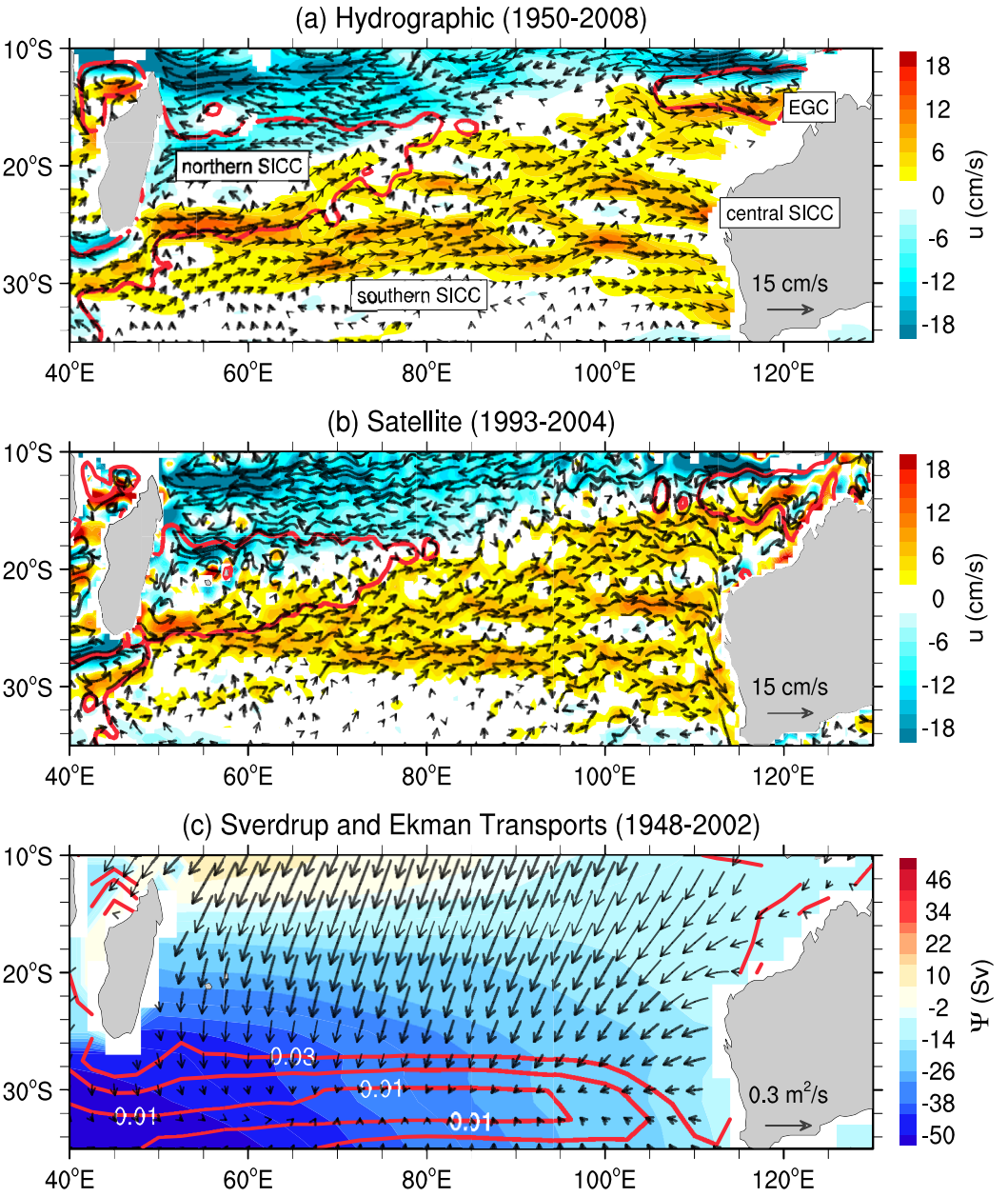

Figure 1. Long-term annual mean surface geostrophic circulation and Sverdrup transport stream function of the South Indian Ocean. (a) Geostrophic circulation relative to 1950 dbar from CARS09 for the period 1950–2008. (b) Absolute geostrophic circulation for the period 1993–2004 from Gravity Recovery and Climate Experiment (GRACE) satellite-based mean dynamic topography (VM08HR). In Figures 1a and 1b, colors represent zonal geostrophic velocities (u). Only vectors with intensities greater than 1 cm/s are plotted. Red contours show the position of the northern cell of the subtropical gyre, east of Madagascar, and the gyre associated with the Eastern Gyral Current (EGC). These contours are the 240 dyn cm of dynamic height from CARS09 (Figure 1a) and 70 cm of absolute dynamic topography (Figure 1b), respectively. (c) Sverdrup stream function (color) and Ekman transport (vectors) for the period 1948–2002 derived from the NCEP (National Centers for Environmental Prediction) Reanalysis winds from *Shi et al.* [2007]. Red contours in Figure 1c depict the region of the wind stress minimum (N/m^2).

Palastanga et al., 2007; *Jia et al.*, 2011; *Kobashi and Kubokawa*, 2012] suggest that the SICC dynamics must be similar to the STCCs.

Kobashi and Kubokawa [2012] define a STCC as a narrow eastward jet on the equatorward side of a subtropical gyre, where the depth-integrated flow is westward as predicted by the Sverdrup theory. The jet accompanies a thermal and a density front, which they call the Subtropical Front (STF), occurring at subsurface depths around 100–200 m. This front gives rise to an eastward shear near the surface by the thermal wind relation. Observational and theoretical studies have shown that the STCC front is tightly related to low

potential vorticity (PV) regions (mode waters) at the pycnocline level and poleward of the front [e.g., *Aoki et al*., 2002; *Kobashi et al*., 2006; *Kobashi and Kubokawa*, 2012, and references therein].

In the South Indian Ocean, however, both the southern and northern branches of the Subtropical Front, also called Subtropical Convergence Front, are located south of 30°S [*Belkin and Gordon*, 1996; *Lan et al*., 2012; *Graham and De Boer*, 2013]. Nevertheless, *Palastanga et al*. [2007] and *Siedler et al*. [2006] conjecture the presence of a secondary density front between 20°S and 30°S possibly caused by a strong meridional salinity gradient east of 75°E and suggest that the SICC might be the jet associated with this salinity front in terms of thermal wind balance. The strong meridional salinity gradient is due to the presence of the fresh waters of the Indonesian Throughflow (ITW) and the salty subtropical waters (STW).

These two different ideas in the literature about the front associated with the SICC (salinity versus thermal front) are probably related to the sparseness of the historical hydrographic observations in the SIO, especially in relation to salinity [e.g., *Roemmich and Gilson*, 2009]. Fortunately, the present-day ongoing Argo program has been collecting globally distributed upper ocean temperature and salinity vertical profiles since 2004 and several climatological atlases have been constructed. We can now use these new data sets to answer the question of whether the SICC is a jet associated with a salinity front as conjectured by *Palastanga et al*. [2007] and *Siedler et al*. [2006] or with a subsurface thermal front like the STCCs.

The objective of the present work is to give a detailed description of the structure of the SICC and associated fronts for the first time, including salinity effects, volume transports, and seasonal variability based on observations. Furthermore, we investigate whether or not the STCC paradigm would also explain the SICC as recently suggested by *Kobashi and Kubokawa* [2012]. This effort lays the groundwork for future studies investigating the formation mechanism and dynamics controlling the SICC.

We find that the SICC is best described as composed of three main branches or jets. The stronger southern branch around 26°S has an associated thermal front at subsurface depths around 100–200 m, with salinity being of secondary importance. Our analysis suggests that the southern branch is related to low-PV regions at pycnocline levels and poleward of the front similar to that related to a STCC-like current. The STCC mechanism, however, does not seem to explain the multiple jet structure (or fine structure) of the SICC, especially its well-defined central branch around 22°S–24°S. The SICC multiple jet structure seems to be more related to the formation of PV staircases in the SIO.

The paper is organized as follows. Sections 2 and 3 describe the observational data sets and analysis used here, respectively. Results are found in section 4, where special attention is given to assess the importance of salinity for the SICC definition as conjectured by *Palastanga et al*. [2007] and *Siedler et al*. [2006]. Section 5 investigates the SICC under two PV paradigms: the STCC (low-PV regions poleward of the front at pycnocline level) and the PV staircase. Section 6 provides a summary of the relevant results of this work.

2. Data

2.1. Climatologies

Three Argo-based temperature and salinity annual mean and seasonal atlases have been analyzed: (1) CSIRO (Commonwealth Scientific and Industrial Research Organisation) Atlas of Regional Seas (CARS09) version 2011.1.0 [*Ridgway et al*., 2002; *Condie and Dunn*, 2006]; (2) the Roemmich-Gilson Argo Climatology 2012 (RG) [*Roemmich and Gilson*, 2009]; and (3) the Monthly Isopycnal and Mixed-Layer Climatology version 2.2 (MIMOC) [*Schmidtko et al*., 2013]. A comparison among these atlases and the WOA09 has been done by *Schmidtko et al*. [2013]. They show that the three atlases analyzed here present less spatial smoothing than WOA09 (World Ocean Atlas 2009) and are thus more suitable to study fronts such as those associated with subtropical countercurrents.

CARS09 is a global atlas of ocean water properties. It is based on a comprehensive set of quality-controlled vertical profiles of in situ temperature (T), practical salinity (S_p), oxygen, nitrate, silicate, and phosphate. The raw profiles belong to different databases that include the (i) Argo global archives up to May 2009, (ii) World Ocean Database 2005, (iii) WOCE (World Ocean Circulation Experiment) hydrographic data, (iv) profiles from TAO/TRITON (Tropical Atmosphere Ocean/Triangle Trans-Ocean Buoy Network) Array moorings, (v) CSIRO Marine and Atmospheric Research and the New Zealand National Institute of Water and Atmospheric Research archives [*Condie and Dunn*, 2006]. Most of these data were collected between 1950 and 2008.

The scattered data were mapped onto gridded fields using a locally weighted least squares quadratic smoother that takes into account the bottom topography and uses an adaptive smoothing scale that depends on the data density [*Ridgway et al*., 2002]. The mapping algorithm also involves simultaneous fitting of annual and semiannual harmonics.

The CARS09 gridded fields cover the region between 0°E and 360°E and 75°S and 90°N, have horizontal grid resolution of 0.5° × 0.5°, and are mapped onto 79 standard depths from the sea surface to 5500 m. Annual harmonics are defined down to 1800 m and the semiannual down to 1000 m. Note that the so-called effective spatial resolution of CARS09 varies over the whole domain due to the variable mapping scales approach [*Ridgway et al*., 2002]. For example, at the surface level, the effective resolution (which is different from the regular grid resolution) ranges from 110 km at the Australian meridional boundaries to more than 550 km in the Southern Ocean.

The RG climatology of T and S_p properties is an atlas derived from quality-controlled vertical profiles obtained only by Argo floats [*Roemmich and Gilson*, 2009]. The RG version used here is based on 8 years of Argo data from 1 January 2004 through 31 December 2011. The RG gridded fields were obtained by a procedure that combines a weighted least squares smoother (first guess) as developed by *Ridgway et al*. [2002] and optimal interpolation. The mapping algorithm is fully described by *Roemmich and Gilson* [2009]. For the optimal interpolation, the covariance function is represented as the sum of a small-scale Gaussian function and a large-scale exponential function. In contrast to CARS09, six temporal harmonics with periods of 2–12 months are fitted. The RG climatology covers the region between 0°E and 360°E and 65°S and 65°N. Two versions for the annual mean fields are available with horizontal grid resolution of 1/6° × 1/6° and 0.5° × 0.5°, respectively. Monthly means are available only with 0.5° × 0.5° resolution. The RG data set is defined at 58 standard pressure levels from the surface to 1975 dbar. We use only the 0.5° × 0.5° RG version to be consistent with CARS09 and MIMOC atlases, although the effective spatial resolution in RG also varies over the whole domain.

The MIMOC is a global atlas of temperature and salinity properties, with horizontal grid resolution of 0.5° × 0.5° from 80°S to 90°N. It is based on quality-controlled vertical profiles mostly obtained from Argo floats up to January 2012, and complemented with ice-tethered profilers and World Ocean Database 2009 archives [*Schmidtko et al*., 2013]. MIMOC is originally computed at isopycnal and mixed layer coordinates using an optimal interpolation procedure that accounts for the influences of bathymetry and latitude [*Johnson et al*., 2012; *Schmidtko et al*., 2013]. The mapping algorithm includes a front-sharpening weighting scheme and data collected before 2007 are de-emphasized by decreasing their signal-to-noise energy in the covariance matrix. After mapping, MIMOC fields in the mixed layer and on each interior ocean isopycnal surface are smoothed with a two-dimensional fifth-order binomial filter and gaps are filled with a spatial third-order binomial filter [*Schmidtko et al*., 2013].

Three MIMOC products are available: (i) conservative temperature and absolute salinity [*IOC et al*., 2010; *McDougall et al*., 2012] fields in the mixed layer, (ii) the same properties mapped on isopycnal layers for the interior ocean, and (iii) potential temperature referenced to 0 dbar (θ) and practical salinity in pressure coordinates. In the present study, we use the pressure-mapped product since it is similar to CARS09 and RG climatologies. The pressured-mapped MIMOC spans from the surface to 1950 dbar at 81 standard pressure levels.

The potential temperature θ at each vertical level for CARS09 and RG climatologies was calculated using the SeaWater (GSW) Oceanographic Toolbox of TEOS-10 (the International Thermodynamic Equation of Seawater 2010) from in situ T and absolute salinity (S_a) [*IOC et al*., 2010; *McDougall and Barker*, 2011]. Conversion between the original S_p to S_a and from depth to sea pressure was performed using the TEOS-10 Toolbox as needed. The toolbox was also used to calculate the density of seawater (ρ), the potential density of seawater (σ_θ), the seawater thermal expansion coefficient (α) with respect to θ and the seawater saline contraction coefficient (β) at constant θ for each climatology described above.

In the present paper, all salinity fields refer to absolute salinity S_a values that now have units of g/kg [*IOC et al*., 2010; *McDougall and Barker*, 2011].

2.2. Hydrographic Data

We analyzed salinity and temperature profiles between 20°S and 32°S from six meridional hydrographic sections collected in (i) 1995 during the WOCE (55°E, 80°E, and 95°E); (ii) 2007 (95°E), and (iii) 2012 and

Table 1. Meridional Hydrographic Sections Analyzed in This Study[a]

Longitude	Vessel	Date	Cruise
54°E30′	R/V Knorr	11 June to 11 July 1995	WOCE section I4–5W-7C
80°E	R/V Baldridge	23 September to 24 October 1995	WOCE section I8NR
95°E	R/V Knorr	24 January to 5 March 1995	WOCE section I09N
95°E	R/V Roger Revelle	27 March to 1 May 2007	CLIVAR/CO2 section I9N
105°E	R/V Southern Surveyor	24 August to 6 September 2012	Voyage ss2012_v04
105°E	R/V Southern Surveyor	10 July to 14 July 2013	Voyage ss2013_v04

[a]Date column refers to the date of occupation of 20°S–30°S.

2013 (105°E) (Table 1). The quality-controlled CTD (Conductivity-Temperature-Depth) data from WOCE and 2007 cruises are available at CLIVAR & Carbon Hydrographic Data Office (http://cchdo.ucsd.edu/indian) and the 2012/2013 cruises at CSIRO Marine and Atmospheric Research Data Centre (http://www.marine.csiro.au/nationalfacility/voyages/datasets.htm).

In all cruises, the CTD stations are typically 55 km apart along the meridional sections and the quality-controlled profiles have a vertical resolution of 2 dbar. We linearly interpolated these data to a common meridional and vertical grid. No extrapolation has been done. The meridional grid was defined from 32°S to 20°S with resolution of 0.2°, and vertical grid from 2 to 2000 dbar with vertical resolution of 2 dbar.

3. Methods of Analysis

3.1. Fronts

Oceanic fronts are narrow bands that separate different water masses. They are marked by sharp changes in the vertical structures and enhanced horizontal gradients of physical, chemical, and biological properties [*Belkin and Gordon*, 1996; *Lan et al*., 2012]. In the present study, we use the traditional gradient-based method to identify the fronts, though more sophisticated methods have been recently developed [*Lan et al*., 2012; *Qiu and Kawamura*, 2012]. The gradient-based method is simple and straightforward, identifying high horizontal gradient values of temperature, salinity, and density associated with fronts. However, because the method is based on the gradient fields, it is very sensitive to errors and noise in the observational data [*Lan et al*., 2012; *Qiu and Kawamura*, 2012]. This disadvantage was circumvented here using the approach formulated by *Anderssen and Hegland* [1999] instead of the classical three-point centered difference scheme (also known as the midpoint formula). The Anderssen-Hegland method takes into account the data dimensionality and uses an averaging scheme to produce a stable numerical differentiation with increased accuracy [see e.g., *Strang*, 2007].

The gradient of a seawater property ∇p at each vertical level is given by

$$w_{i,j} = \sum_{k=-r_1}^{r_1} \sum_{m=-r_2}^{r_2} p_{i+m,j+k} \tag{1}$$

$$\left.\frac{\partial p}{\partial x}\right|_{i,j} = \frac{w_{i,j+s_2} - w_{i,j-s_2}}{2(2r_1+1)(2r_2+1)s_2 d} \tag{2}$$

$$\left.\frac{\partial p}{\partial y}\right|_{i,j} = \frac{w_{i+s_1,j} - w_{i-s_1,j}}{2(2r_1+1)(2r_2+1)s_1 d} \tag{3}$$

where p represents a seawater property (temperature, salinity, or density), w is the sum of p used in the averaging, x and y are the eastward and northward coordinates as usual, respectively, d is grid resolution, i and j are row and column indices, respectively, r_1 and s_2 control the averaging in the x direction and r_2 and s_1 control the averaging in the y direction (dimensionless parameters). By applying this two-dimensional spatial neighborhood averaging method for numerical differentiation, one obtains a stable scheme with the increased accuracy of O(d) [*Anderssen and Hegland*, 1999]. Because the South Indian Ocean currents and fronts away from continental shelves are predominantly zonal, we chose an anisotropic set of parameters ($r_1 = s_2 = 3$ and $r_2 = s_1 = 1$), meaning that the derivatives have been estimated using 10 points (7 points in the x direction and 3 points in the y direction). These values were reached after a couple of tests in which we

tried to balance the reduction of the noise and the smoothing in the front strength. In the present work, we focus on the meridional gradients since the SICC is mostly zonal.

The Anderssen-Hegland method was also used to estimate vertical and meridional gradients from the hydrographic sections, but in this case r_1 and s_2 control the averaging in the z direction and r_2 and s_1 control the averaging in the y direction. We chose an isotropic set of parameters ($r_1=s_2=3$ and $r_2=s_1=3$). Recall that the hydrographic sections have a resolution of 0.2° in latitude and the atlases are defined on a 0.5° × 0.5° grid.

3.2. Temperature and Salinity Effects on Density

To evaluate the relative effect of temperature and salinity on density, the horizontal density ratio (R^h) and respective Turner angle (T_u) [*Tippins and Tomczak*, 2003] have been computed for each vertical level from the potential temperature θ and absolute salinity (S_a) fields. R^h is given by $\alpha\Delta\theta/\beta\Delta S_a$, where $\Delta\theta$ and ΔS_a are the changes in potential temperature and absolute salinity over a fixed horizontal distance in the zonal or meridional directions. Since the SICC is mostly zonal, we focus on the meridional density ratio and respective T_u. Thus, $\Delta\theta$ and ΔS_a are computed along meridians over a 0.5° distance (grid spacing). A value of $R^h=1$ means that the salinity and temperature effects on density cancel each other, the compensation phenomenon that occurs in certain fronts (e.g., a horizontal front formed by cold and fresh waters on one side and warm and salty waters on the other) [*Rudnick and Ferrari*, 1999]. A $R^h=2$ means that the effect of temperature on density is twice and opposite to that of salinity while $R^h < 1$ means that the salinity effect is more important. Although the interpretation of R^h is straightforward, it is very sensitive to ΔS_a and R^h goes to infinity when ΔS_a vanishes. To reduce this problem, *Rudnick and Martin* [2002] and *Tippins and Tomczak* [2003] introduced the horizontal Turner angle defined as $T_u=arctan(R^h)$ with $-\pi/2 \le T_u \le \pi/2$. In this case, a density compensation occurs when $|T_u|= 45°$. Salinity gradients dominate the density variations when $|T_u| \ll 45°$, and temperature gradients when $|T_u| \gg 45°$. Hereafter, T_u refers to meridional Turner angles.

3.3. Temperature and Salinity Contributions to the SICC

By the thermal wind relation, geostrophic currents are related to horizontal gradients of density, and so to the horizontal gradients of temperature and salinity. Assuming a linearized equation of state for seawater, the thermal wind relation can be written as [e.g., *Gill*, 1982]

$$\frac{\partial \boldsymbol{v}}{\partial z}=\frac{g}{f}\boldsymbol{k}\times(\alpha\nabla\theta-\beta\nabla S) \tag{4}$$

where $\boldsymbol{v}=u\boldsymbol{i}+v\boldsymbol{j}$; u, v are the zonal and meridional components of geostrophic currents; $\boldsymbol{i},\boldsymbol{j},\boldsymbol{k}$ are the unit vectors; $\nabla=\boldsymbol{i}\partial/\partial x+\boldsymbol{j}\partial/\partial y$ is the horizontal gradient; x, y, and z are the eastward, northward, and upward coordinates as usual, respectively, g is gravity, and f is the Coriolis parameter.

The horizontal gradient has been estimated using the Anderssen-Hegland scheme as described above. Velocity $\boldsymbol{v}(z)$ is then computed in the usual way by integrating equation (4) upward from a reference level of assumed no motion (z_{ref}). Since MIMOC is defined down to 1950 dbar, we used this level as the level of no motion z_{ref} = 1950 dbar. Based on water mass properties, *Stramma and Lutjeharms* [1997] found that density surface $\sigma_2=36.94$ (depth range 1500–2500 m) in the Indian Ocean is an adequate z_{ref} for the geostrophic computation in the subtropical region, north of 40°S. This surface lies below the oxygen minimum layer and above the Circumpolar Deep Water [*Stramma and Lutjeharms*, 1997]. We have computed geostrophic currents using other values of z_{ref} (1000 dbar, 1500 dbar, and 3000 dbar [only for CARS09]), and their patterns are very similar (not shown). Thus, the choice of z_{ref} does not affect the conclusions discussed in the present work.

Considering the temperature and salinity gradients separately, we can use the thermal wind relation to evaluate the contribution of salinity and temperature to the vertical shear of zonal geostrophic velocities, as done by *Menezes et al.* [2013]. The vertical shear of u due to temperature is given by $\partial u_T/\partial z=(-g\alpha/f)\partial\theta/\partial y$ and that due to salinity is given by $\partial u_S/\partial z=(g\beta/f)\partial S/\partial y$. The vertical integration of $\partial u_T/\partial z$ and $\partial u_S/\partial z$ from z_{ref} then gives u_T and u_S. The relative contribution from temperature and salinity to the SICC can be evaluated as $r_T=u_T/u$ and $r_S=u_S/u$, respectively, where u is the total zonal geostrophic velocity based on density, u_T includes only temperature, and u_S only salinity effects. To give percentages of temperature and salinity contributions, the ratios $r_T(r_S)$ are multiplied by 100. Values of $r_S(r_T) > 100$ mean that the

temperature (salinity) acts to reduce the eastward shear (opposite effect on density, see equation (4)). Values of $r_T(r_S) \leq 0$ mean that temperature (salinity) contributes to westward shear.

3.4. SICC Volume Transport

From zonal geostrophic velocity fields referenced to 1950 dbar computed as described above, the annual mean and seasonal SICC zonal volume transports were estimated for each atlas. The zonal volume transport in a section crossing the x zonal position is given as $U(x)=\int_{y_1}^{y_2}\int_{z_1}^{z_2} u(x,y',z')dy'dz'$, where $U(x)$ is the zonal transport in Sv (1 Sv $\equiv 10^6 \mathrm{m}^3/\mathrm{s}$), y_1, y_2 represent the latitudinal limits, and z_1, $z_2=0$ m represent the depth limits of integration. To estimate only the eastward transports (SICC), we first constructed masked u data sets that only include eastward zonal velocities at the surface. The z_1 limit was then determined as the depth where the zonal velocity changes from positive to negative, or 300 m, whichever is deeper. We chose 300 m here because this is the depth range of the thermal front associated with the SICC, as will be discussed later. The limits of integration y_1 and y_2 were roughly determined according to the SICC branch meridional intervals, as will be shown in section 4.

3.5. Auxiliary Parameters: Mixed Layer and Thermocline Depths

Annual mean and seasonal mixed layer depth (MLD) fields for each atlas were determined through the diagnostic method, i.e., as the depth at which the potential density changes by 0.125 kg m^{-3} relative to that at the surface [*de Boyer Montegut et al*., 2004]. We also calculated two estimates of thermocline depth for the annual mean and seasonal fields given by (i) the depth of the maximum vertical gradient $\partial\theta/\partial z$ and (ii) the depth of maximum Brunt-Väisala frequency ($N^2=\frac{-g}{\sigma_\theta}\frac{\partial\sigma_\theta}{\partial z}$, where $g=9.8\mathrm{m}/\mathrm{s}^2$, σ_θ is potential density, and z is depth). Here $\partial\theta/\partial z$ and $\partial\sigma_\theta/\partial z$ have been estimated using centered finite differences. Differences between thermocline depth estimates might be related to temperature and salinity effects, since N^2 depends on vertical density gradients.

4. Results

4.1. Multiple SICC Branches

In the annual mean surface geostrophic circulation maps referenced to 1950 dbar from CARS09 and RG, the SICC can be described as composed of three main distinct cores, which are embedded in a broad and weak eastward flow that dominates the region south of 20°S. These cores are particularly distinct east of 80°E. For example, Figure 1a shows the surface annual mean geostrophic circulation pattern referenced to 1950 dbar from the CARS09 atlas, which is very similar to that obtained from RG (not shown). Hereafter, we will refer to these cores as SICC branches.

In the annual mean surface geostrophic circulation maps from CARS09 and RG, the SICC originates near the southern tip of Madagascar around 25°S–50°E as a relatively strong and well-organized jet with intensities between 9 and 14(18) cm/s in CARS09 (RG) and width around 3.5° in latitude. It flows on the southern limb of the northern cell of the subtropical gyre (red contour in the western basin of Figure 1a). Recall that the subtropical gyre in the SIO has a double-cell structure (supporting information Figure S1) [*Palastanga et al*., 2007, 2009]. The southern recirculation cell is located in the south-western corner of the SIO, west of the Madagascar Ridge, and has the Agulhas Current flowing on its western flank [e.g., *Stramma and Lutjeharms*, 1997; *Palastanga et al*., 2007]. As noted by *Schott et al*. [2009], the SICC seems to be partly supplied by a source farther to the west, which in CARS09 and RG is the Agulhas Return Current (not shown) [e.g., *Lutjeharms and Ansorge*, 2001].

Just on the Central Indian Ridge (65°E–68°E at 25°S), the SICC splits into two main branches: a weaker northern SICC branch with maximum intensity around 4–5 cm/s and a stronger southern branch (8–12 cm/s) (supporting information Figure S2). While the northern SICC continues to flow on the southern limb of the northern cell of the subtropical gyre, the southern branch flows with a slightly poleward slant (26°S–28°S). Notice that the northern cell of the gyre has a roughly elliptical shape, with the major axis tilting slightly equatorward (e.g., see supporting information Figure S1). This cell is embedded in a zonally slanted mean dynamic height (MDH) ridge between Madagascar and the Indonesian Throughflow region (not shown) [but see *Vianna and Menezes*, 2010, Figure 1]. The southern limb of the northern cell begins at the Madagascar shelf at 25°S and ends near the Ninety East Ridge (≈88°E) around 18°S–16°S (in Figure 1 and supporting information Figure S1) [see also *Schott et al*., 2009, Figure 5a]. The reason for the existence of

the slanted recirculation cell east of Madagascar and the MDH ridge is still to be determined [*Palastanga et al*., 2007, 2009; *Schott et al*., 2009].

Flowing on the southern limb of the northern cell of the subtropical gyre, the northern SICC branch has an equatorward slant orientation, particularly east of 70°E. Aiming at a better visualization of this branch, that is difficult to distinguish in Figure 1a, supporting information Figures S1 and S2 show, respectively, the CARS09 surface mean dynamic height referenced to 1950 dbar overlaid with the surface circulation pattern associated with the northern cell and a zoom in the circulation pattern of the western basin. Part of the northern SICC seems to recirculate into the westward-flowing South Equatorial Current (SEC), and part seems to merge with the tropical EGC around 15°S–100°E as already described by *Schott et al*. [2009]. The tropical EGC flows eastward on the southern flank of the tropical Eastern Gyre, which is also embedded in the MDH ridge described before (see supporting information Figure S1).

From the Central Indian Ridge to 75°E, the southern SICC branch between 26°S and 30°S is quite regular and robust with intensities of 7–11 cm/s (Figure 1a). Between 75°E and 80°E, the southern SICC suffers a series of bifurcations and part of the flow goes slightly equatorward to form the central SICC branch around 22°S (supporting information Figure S2). Then, the central SICC flows with poleward slant between 25°S and 22°S and intensities around 6 cm/s, being distinct from the southern branch east of 75°E–80°E (supporting information Figure S3).

Hereafter, we consider the well-organized jet of the SICC west of the Central Indian Ridge as being part of the southern branch because, as we will show in the next section, the front associated with the southern branch begins near Madagascar. Thus, despite the bifurcation/merging observed on its northern limb, the southern SICC flows almost zonally from Madagascar to the west of Australia around 26°S, with a slight poleward orientation. Note that north-eastward flows originating from the South Indian Ocean Current around 40°S (not shown) [e.g., *Stramma*, 1992] seem to present a confluence with the southern SICC branch as already described by *Palastanga et al*. [2007].

A similar triple-core SICC pattern is identified in CARS09 and RG maps whether the reference level is 1000 dbar, 1500 dbar, or 3000 dbar (only for CARS09) (not shown). It should be noted, however, that the MIMOC atlas does not show this triple-core pattern: it only shows a broad eastward flow with enhanced velocities in the southern SICC (5–10 cm/s), which can be identified in the region south of 20°S (not shown). This lack of sufficient resolution is probably caused by the low-pass binomial spatial filter applied to the production of the MIMOC fields (see section 2.1.). Despite the smoothness of the surface geostrophic current field, MIMOC is able to capture the differences between the thermal fronts associated with the branches. This is one reason why we also analyze the MIMOC atlas in the present work.

Siedler et al. [2006] have already described the SICC as strong and well defined between Madagascar and 80°E and becoming broader east of this meridian, based on a 5 year average surface geostrophic circulation from satellite altimetry. Moreover, *Divakaran and Brassington* [2011] describe the surface circulation in the eastern basin (east of 90°E) as resembling an arterial-like structure. To verify that the triple-core pattern of the SICC observed in CARS09 and RG can be identified in satellite products, we have analyzed several different pure geodetic and hybrid satellite-derived absolute Mean Dynamic Topography (MDT) products (VM08-HR, CLS09, VMC07, Maximenko-Niiler04, JPL08, DNSC08, and Rio05, see *Vianna and Menezes* [2010] for a complete description of these MDTs). Similar triple-core patterns can be identified in all the surface geostrophic circulation fields derived from those products, although the core speeds vary among them. For example, Figure 1b shows the absolute surface geostrophic circulation derived from the geodetic VM08-HR MDT. This MDT product has a 0.1° grid resolution and is based on the DNSCMSS08 (Danish National Space Center) Mean Sea Surface and the Earth Gravitational Model 2008 (EGM08) [*Vianna and Menezes*, 2010]. No in situ oceanographic data have been used in the VM08-HR computation. Note the similarity between the surface circulation patterns from Figures 1a and 1b, which are based on two completely independent data sources: hydrography (referenced to 1950 dbar) and satellite MDT (absolute). Thus, the SICC pattern composed of a triple-jet structure seems to be strongly independent of the time average period considered, and also not dependent on the MDT model used: it seems to be a robust mean structure, resembling the structure of eastward flows observed in other oceans (e.g., the STCC in the North Pacific Ocean) [*Kobashi et al*., 2006; *Vianna and Menezes*, 2010; *Kobashi and Kubokawa*, 2012].

A vertical section of annual mean zonal geostrophic velocities from CARS09 and RG in the region where the three SICC cores begin to be particularly distinct, between 75°E and 85°E, indicates that the central SICC

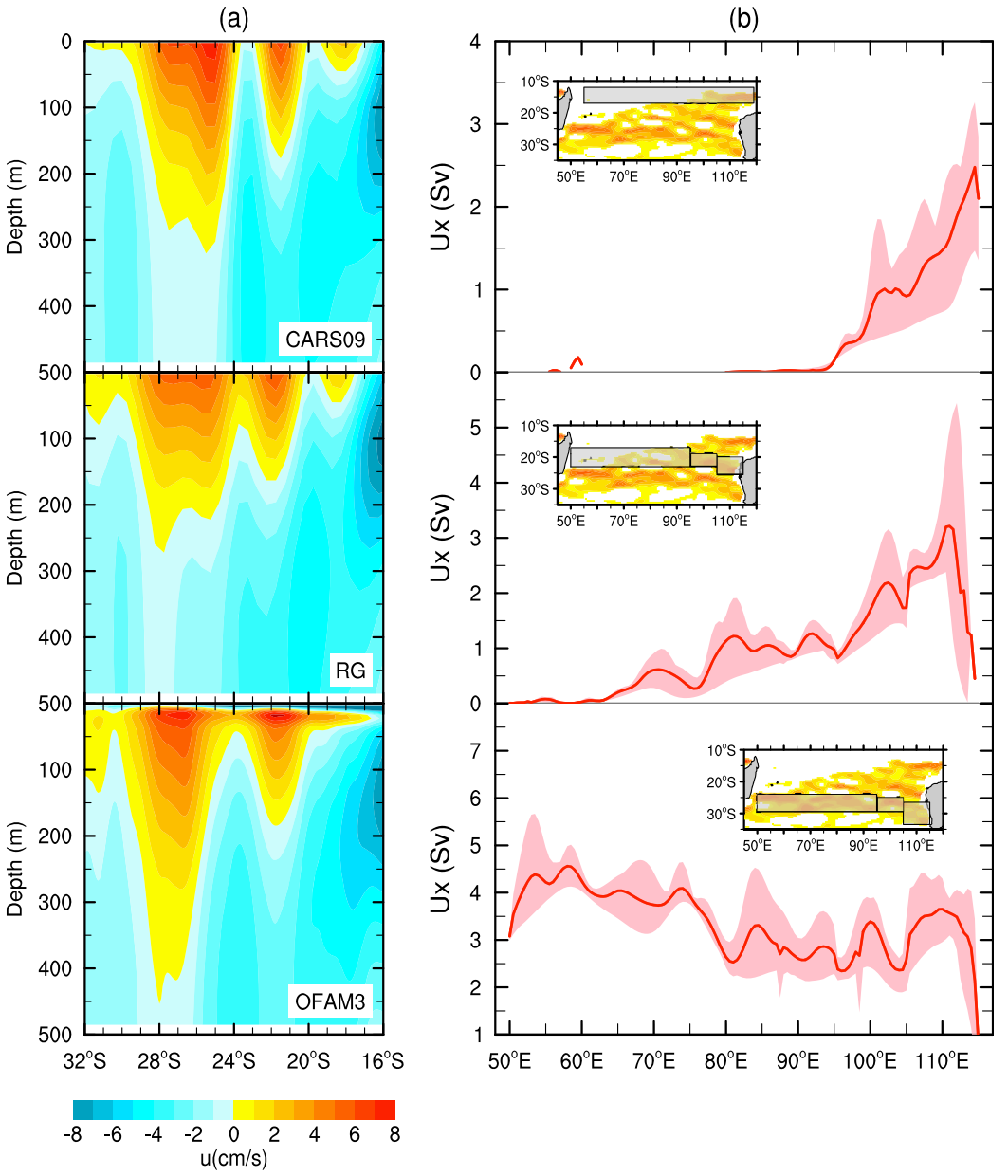

Figure 2. Vertical sections of annual mean zonal velocities averaged between 75°E and 85°E (a) showing the 3 SICC branches. (b) Eastward volume transports (U_x) 0/300 m in Sverdrups averaged from CARS09, RG, and MIMOC (1 Sv $\equiv 10^6 m^3/s$), the top figure referring to the EGC, middle figure to the cSICC and nSICC branches, and bottom to the sSICC. Pink shadings show the respective minimum/maximum eastward transports and maps indicate the *y* range of integration at each longitude *x* (see text for details).

branch is shallower (150 m) than the southern SICC (300–350 m) (Figure 2a). In both CARS09 and RG, the northern SICC is weak ($u \approx$ 1–3 cm/s) and confined to the upper 50 m, mostly inside the mixed layer. Below these eastward currents, the flow is westward. In MIMOC, only a broad eastward flow exists between 20°S and 32°S and is strongest ($u \approx$ 7 cm/s) at 26°S (not shown). For a qualitative comparison, we have plotted a similar vertical section of the total zonal velocities averaged between 1993 and 2010 from outputs of the 1/10° grid resolution eddy-resolving model OFAM3 (Ocean Forecasting Australia Model, nondata assimilated) [*Oke et al.*, 2013]. The pattern in OFAM3 is similar to that obtained from CARS09 and RG with the central SICC being shallower (≈180 m) than the southern SICC (≈450 m) (Figure 2a). Note that the northern SICC does not clearly appear in OFAM3 probably because this geostrophic current, being very shallow and weak, is masked by the westward Ekman component of the model in the first 10–20 m.

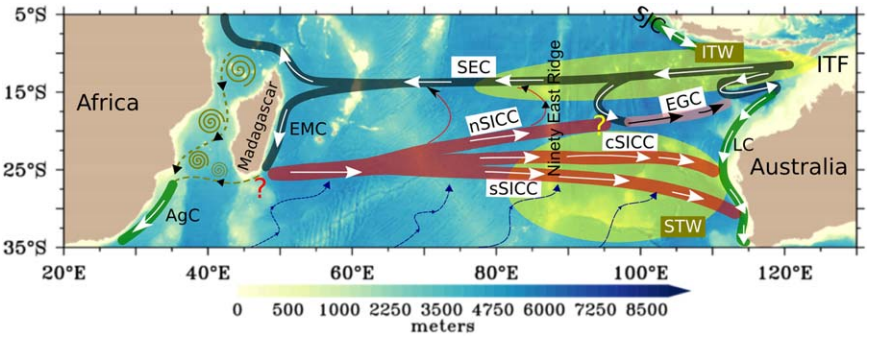

Figure 3. Schematic representation of the upper layer circulation of the South Indian Ocean based on Figure 1. Currents indicated are the three branches of the South Indian Countercurrent (northern [nSICC], central [cSICC], and southern [sSICC]), the South Equatorial Current (SEC), the East-Madagascar Current (EMC), Agulhas Current (AgC), the seasonally reversing South Java Current (SJC), the Eastern Gyral Current (EGC), and the Leeuwin Current (LC). Question marks (?) indicate regions where the circulations are still a matter of debate: the retroflection of the EMC and its connection to the SICC, and the connection between the SICC and the tropical EGC. Spirals indicate the southward-propagating Mozambique Channel eddies. Yellow shadings show the Indonesian Throughflow Water (ITW) and the subtropical Water (STW) regions. ITF stands for the Indonesian Throughflow. Water depths are blue shadings from the Smith-Sandwell 2 min bathymetry.

In this study, we have estimated for the first time the annual mean eastward volume transports 0/300 m for each SICC branch. Figure 2b shows the eastward transports of each branch averaged between the three atlases (red curves) and the minimum/maximum values (shadings). Note that the SICC branches are shallower than 300 m on average (Figure 2a), and the limits of integration y_1 and y_2 for the transport calculation vary with longitude as described in section 3.4. These limits were roughly determined according to the meridional intervals of the SICC branches based on Figure 1a (CARS09). The boxes in the maps of Figure 2b show the different *y*-limits of integration.

The southern SICC has an annual mean eastward volume transport around 4 Sv from 50°E up to 75°E; east of this meridian, the transport is slightly lower (≈3 Sv) (Figure 2b, bottom). The northern and the central SICC transports are shown in Figure 2b (middle). Note that from 65°E to 80°E, the eastward transport shown in this part is that of the merged northern and central SICC branches, being less than 1 Sv. East of 80°E, the volume transport of the central SICC increases and reaches a maximum of 5 Sv (in RG) around 110°E (3 Sv in CARS09 and 2.4 Sv in MIMOC). The eastward transport for the EGC is on the top and varies from $<$0.5 Sv at 95°E to 2–3 Sv at 110°E.

Based on the surface geostrophic maps obtained from satellite and hydrographic data, including CARS09 and RG, and the analysis of the subsurface structure of these branches, we have drawn a more detailed schematic diagram of the large-scale upper ocean mean circulation of the SIO in which the three branches of the SICC appear explicitly (Figure 3). We refer to these branches as the northern (nSICC), the central (cSICC), and the southern SICC (sSICC).

4.2. Subsurface Thermal Front Associated With the Southern SICC

Analysis of the annual mean meridional gradients of potential temperature ($\partial\theta/\partial y$) from CARS09, RG, and MIMOC shows that in the southern SICC region the highest positive gradients are found between 150 and 250 m (Figure 4, left). In the southern hemisphere ($f < 0$), eastward shear arises from positive (negative) meridional gradients of temperature (salinity). Hereafter in this section, we will refer to the meridional gradients of potential temperature as simply temperature gradients. Note that in the figure, we have used colored vectors to facilitate the identification of two SIO eastward flows: the subtropical SICC (south of 20°S) and the tropical EGC (between 15°S and 20°S, and east of 90°E). For details about the EGC, see *Menezes et al*. [2013, and references therein].

Data from the three atlases analyzed here show a similar distribution of the depth of maximum $\partial\theta/\partial y$ (Figure 4, left). The distribution is characterized by a band between 23°S and 28°S extending from Madagascar to the west of Australia with maximum temperature gradients around 150–250 m (green color in Figure 4, left). Notice that this band is almost collocated with the southern branch of the SICC, indicating that a subsurface thermal front might exist there. Outside this band, maximum temperature gradients occur at shallower depths ($<$75 m), except near 10°S. In the southern SICC region, the MLD is shallow in the western

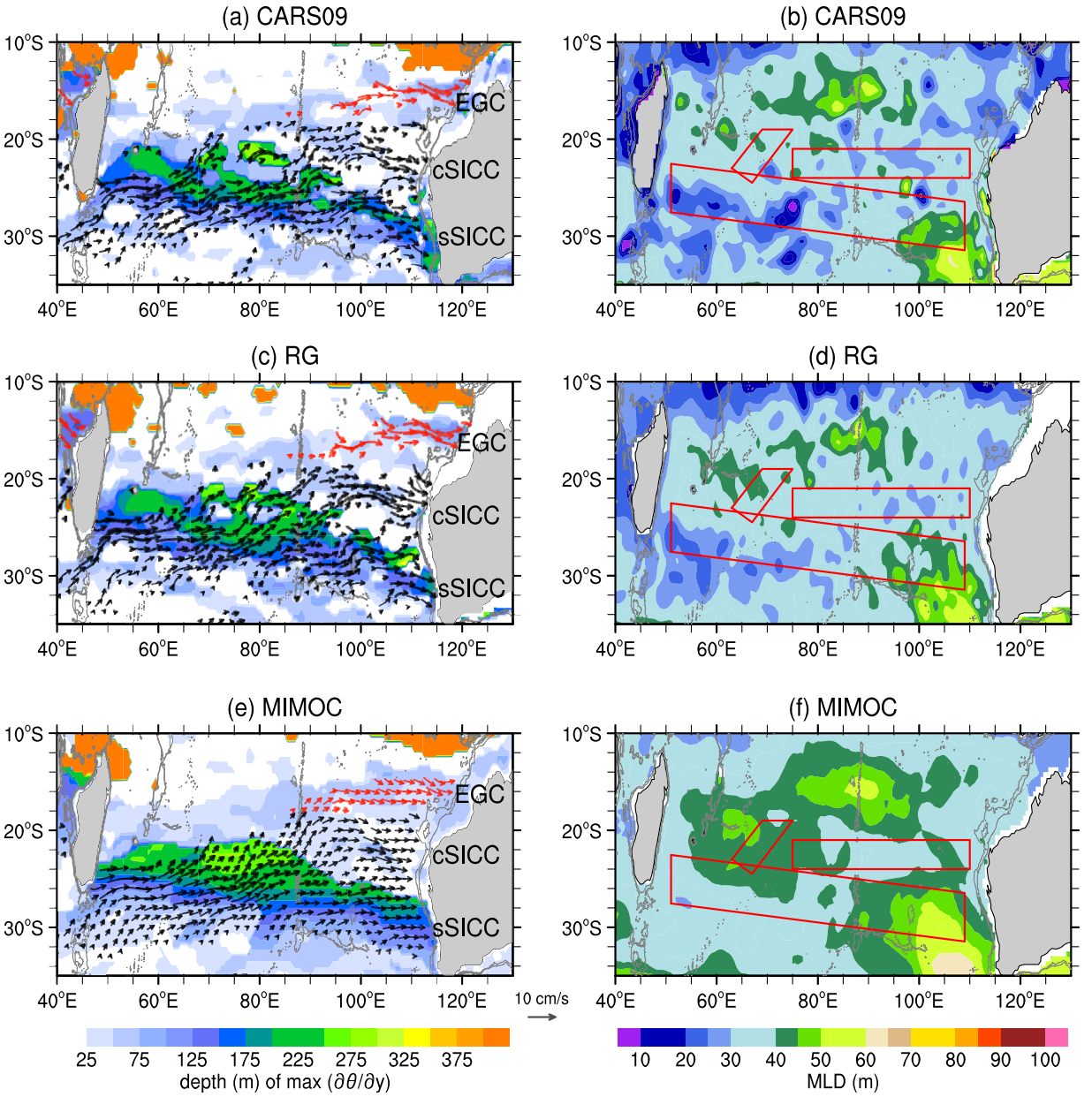

Figure 4. (left) Depth (m) at which the meridional gradient of potential temperature ($\partial\theta/\partial y$) is maximum in the annual mean fields. Black/red vectors are the eastward geostrophic currents at the surface referenced to 1950 dbar. Vectors are only plotted for currents with intensities greater than 1.5 cm/s. Black vectors are used for the SICC and red vectors for the EGC. EGC is the eastward current between 15°S and 20°S, east of 90°E and SICC denotes the eastward flows south of 20°S. (right) Annual mean mixed layer depth (MLD). Gray contours are the 2000 m and 3000 m isobaths from Smith-Sandwell 2 min bathymetry. cSICC (sSICC) stands for the central (southern) SICC branch. The boxes indicate the areas corresponding to the SICC branches. The sSICC is within the southern rectangle with a slightly poleward slant and the cSICC is within the central zonal rectangle. The polygon with the marked equatorward slant centered near 70E only indicates the region where the nSICC is strongest.

basin (20–30 m) and deeper in the eastern basin, reaching 50–60 m east of 95°E (Figure 4). While CARS09 and RG have similar MLD, MIMOC presents deeper mixed layers with a spatial distribution different from the other atlases. These differences are probably related to the technique used for the MIMOC construction. In MIMOC, the mixed layer is treated separately from the interior ocean isopycnal maps and merged a posteriori [*Schmidtko et al.*, 2013], while in CARS09 and RG the data are mapped directly in pressure coordinates [*Ridgway et al.*, 2002; *Condie and Dunn*, 2006; *Roemmich and Gilson*, 2009].

Temperature gradients at 10 m (mixed layer), 200 m, and 600 m are shown in Figures 5a–5c only for CARS09. Visual inspection shows that the three climatologies have consistent spatial patterns and similar

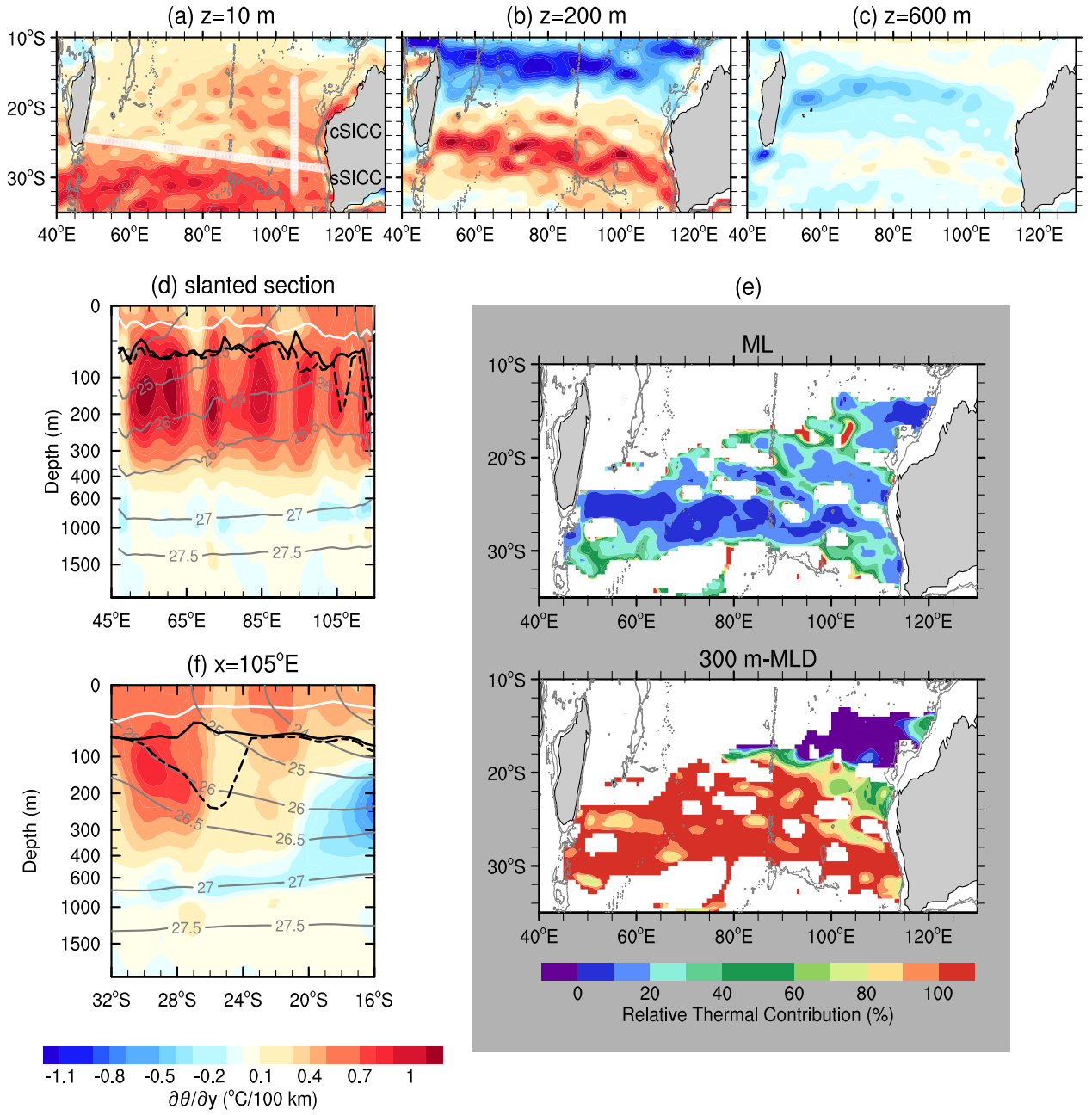

Figure 5. Annual mean meridional gradient of potential temperature ($\partial\theta/\partial y$) from CARS09 at (a) 10 m, (b) 200 m, and (c) 600 m. White lines show the position of the sections plotted in (d, f). In Figure 5d, $\partial\theta/\partial y$ along the slanted section (no average). In Figure 5f, along 105°E (averaged between 102.5° and 107.5°E). Contours in Figures 5d and 5f are (i) the isopycnals σ_θ =24, 25, 26, 26.5, 27, and 27.5 (gray), (ii) the mixed layer depth (white), (iii) the depth of the maximum $\partial\theta/\partial z$ (dashed black), and (iv) the depth of maximum Brunt-Väisala frequency (black). The latter contours have been smoothed with a three-point running mean in longitude (≈1.5°) to reduce the noise. (e) Relative thermal contribution (%) for the annual mean surface eastward currents (see text for details). Negative values (purple) indicate that the layer contributes to westward shear. Gray contours in the maps are the 2000 m and 3000 m isobaths from Smith-Sandwell 2 min bathymetry. cSICC (sSICC) stands for the central (southern) SICC branch.

temperature gradient values, although gradients are smoother in MIMOC (not shown). To evaluate quantitatively the spatial consistency between the θ fields from the three atlases, we have analyzed them using Empirical Orthogonal Functions (EOF) in a similar way as done in *Vianna and Menezes* [2010] for comparing different MDT products. For this analysis, the annual mean CARS09 and MIMOC fields have been linearly interpolated onto the same 58 standard *z*-levels as RG. Then, for each standard *z*-level, the triplet θ fields (CARS09, RG, and MIMOC) were expanded into three EOF modes. The first EOF mode gives the triplet correlation by its maximum total variance, and the best correlated map, while the second/third modes give the

residual map corresponding to each triplet. We found that the variance explained by the leading mode slightly decreases with increasing depth. It varies from 99.8% (surface) to 98.7% (1700 dbar), with average value of 99.3% and standard deviation of 0.29%. At 10 m, the variance explained by the leading mode is 99.7% and 99.5% at 200 m and 600 m. Thus, most figures hereafter are based on CARS09, which incorporates both historical hydrographic and Argo data, unless specified.

In the mixed layer, the region with the highest temperature gradients (≈0.8°C/100 km) extends zonally from the western basin to 100°E, south of 30°S, and corresponds to the North Subtropical Front described by *Belkin and Gordon* [1996]. Relatively high temperature gradients (0.4–0.6°C/100 km) can also be seen east of the Ninety-east Ridge (≈88°E) between 20°S and 30°S (Figure 5a). These high gradients are almost collocated with the central SICC branch (not shown). The spatial distribution of temperature gradients at 10 m presented here is very consistent with that computed by *Palastanga et al*. [2007] based on WOA01 and by *Lan et al*. [2012] from time-averaged microwave satellite-derived SSTs.

At 200 m, two quasi-zonal thermal fronts crossing the basin are clearly identified (Figure 5b), one with negative and the other with positive gradients. The thermal front with negative gradients (<-1.1°C/100 km) extends from the Indonesian Throughflow (not shown in Figure 5b) to Madagascar between 10°S and 18°S and is associated with the westward-flowing SEC. The front with positive gradients (>0.9°C/100 km) extends from Madagascar to the west of Australia around 26°S. This subsurface front is characterized by a meandering pattern, very clear in MIMOC (not shown), and has a slightly poleward slant. The front lies in the 150–250 m band shown in Figure 4 (left), being almost collocated with the southern branch of the SICC. Positive gradients (0.2–0.5°C/100 km) are also found in the region where the northern and central SICC branches flow, but not in the EGC region where the temperature gradients are indeed negative (westward vertical shear).

The subsurface thermal front around 26°S is a distinct feature with strong positive gradients (0.8–1.3°C/100 km) from 125 m to 300 m in the three atlases. From 350 m downward, the front weakens and almost vanishes around 600 m (Figure 5c), although a very weak positive signal can still be detected ($\partial\theta/\partial y <$ 0.1°C/100 km).

The vertical structure of temperature gradients along a poleward-slanted section (white line in Figure 5a) is shown in Figure 5d. This section was selected to roughly follow the subsurface thermal front axis and extends from Madagascar (24°S; 48°E) to the west of Australia (29°S; 116°E). In this section, the strongest positive gradients (>1°C/100 km) are found between 100 and 250 m. These strong positive gradients (eastward shear) are located in the thermocline level above the $\sigma_\theta=26.5$. From 300 m to 600 m, the temperature gradients progressively weaken, becoming negative (westward shear) around 800–1000 m ($\sigma_\theta=27$). Note that although the vertical section from MIMOC is very consistent with CARS09 and RG, the $\sigma_\theta=27.5$ level in MIMOC is shallower (≈1000 m depth) than those obtained in the other atlases (≈1400 m) (not shown). This is a known feature in MIMOC where the densest isopycnals are biased toward shallow pressures relative to other atlases [*Schmidtko et al*., 2013]. It is probably because of this characteristic that the correlation between the three atlases, which is given here by the variance of the leading EOF mode, drops below 1000 m (from 99.1% to 98.7%).

To determine whether the southern SICC is associated with the subsurface thermal front described above, in terms of thermal wind balance, the vertical shear of zonal velocities due to temperature $(\partial u_T/\partial z)$ (see section 3.3) was integrated from 300 m upward to the MLD giving u_{Ttherm}. Similarly, the contribution of the mixed layer was estimated by integrating $\partial u_T/\partial z$ from the MLD upward to the surface (u_{Tml}). The relative contribution to the current from mixed layer and thermocline depths can then be evaluated as $r_{Tml}=u_{Tml}/u$ and $r_{Ttherm}=u_{Ttherm}/u$, respectively, where u is the total zonal velocity at the surface referenced to 1950 dbar computed from the density fields. Thus, the relative contribution of u_{Ttherm} and u_{Tml} depends on the local thickness of the mixed layer. To give percentage contribution, the ratios r_{Tml} and r_{Ttherm} were multiplied by 100. Notice that $r_{Tml}(r_{Ttherm}) > 100$ means that another depth range (or salinity) reduces the eastward shear and $r_{Tml}(r_{Ttherm}) \leq 0$ means that the layer (mixed layer or thermocline depths) contributes to westward shear.

In the three atlases, more than 80% of the southern SICC intensity at the surface arises from the eastward shear due to the subsurface thermal front (e.g., Figure 5e for CARS09). In both CARS09 and RG, the mixed layer contributes a maximum of 20% for the southern SICC while in MIMOC it reaches 30–40% in the

eastern basin (not shown), probably because the MLD in MIMOC is deeper in this region (Figure 4, right). To evaluate the uncertainty associated with the split between the mixed layer and the subsurface contributions, which depend on the local thickness of the mixed layer, we have also estimated u_{Ttherm} and u_{Tml} (and respective ratios) using the deeper MIMOC MLD as reference. Whether the MIMOC MLD is used in the calculations, we find the mixed layer contribution being roughly 6–8% greater than that shown in Figure 5e. The root-mean square of the difference between the mixed layer contribution using MIMOC as reference and using CARS09 (RG) is 5.8% (5.2%). Thus, the choice of the MLD product does not affect the conclusions discussed in the present work. In the southern SICC, the sum of the mixed layer and the thermocline contributions gives more than 100%, which means that temperature gradients from another depth range (below 300 m) or salinity gradients contribute to westward shear.

In the western basin up to the Ninety-east Ridge, the thermocline front is the major contributor to the SICC. In the eastern basin, there is a transition zone, with the subsurface layer becoming gradually less important around the central SICC region (Figure 5e, bottom). Notice that in the EGC region, the subsurface layer does not contribute to eastward shear ($r_{Ttherm} < 0$). *Menezes et al*. [2013] have studied this regional feature and showed that in the EGC region, the salinity gradients overwhelm the contribution from temperature gradients to density gradients, generating an eastward geostrophic shear and establishing the EGC.

4.3. Thermal Structure of the cSICC and sSICC Branches

To examine the differences between the central and southern SICC in relation to their respective fronts in more detail, the vertical distribution of the temperature gradients along 105°E, averaged across a $\pm 2.5°$ band, has been calculated (Figure 5f). This section has been chosen because in the eastern basin the two branches (cSICC and sSICC) are very distinct.

In the southern SICC domain (south of 25°S), the strongest positive gradients are found in thermocline levels between 100 and 200 m ($\sigma_\theta = 26.0 - 26.5$), as described before. In the central SICC domain (24°S–21°S at 105°E), the strongest positive gradients are weaker (0.5–0.7°C/100 km) and confined to $\sigma_\theta \leq 25$. Although in MIMOC, we cannot identify two distinct SICC branches in the geostrophic field, the temperature gradients show a similar pattern as observed in CARS09 and RG (not shown). The core of positive temperature gradients in the southern SICC domain is also deeper, located at thermocline depths (100–200 m).

4.4. Salinity Effect on Density and the SICC

The spatial coherence of salinity fields between the three atlases was first evaluated by an EOF analysis as done for the θ fields. The salinity fields of the three atlases were found to be highly correlated, with the variance explained by the leading EOF mode varying from 98% to 99.5%, with an average value of 99% and standard deviation of 0.43%. Thus, most figures in this section are also based on CARS09.

The annual mean meridional gradients of salinity in the mixed layer and at 200 m depth are shown in Figures 6a and 6b. Negative meridional gradients of salinity give rise to eastward shear in the southern hemisphere ($f < 0$). Hereafter in this section, we will refer to the meridional gradients of salinity as salinity gradients.

In the mixed layer (Figure 6a), the salinity gradients are negative almost everywhere except south of 30°S. At 200 m depth (Figure 6b), the salinity gradients are positive in the southern SICC region and negative north of 22°S. The positive gradients around 26°S form a quasi-zonal front-like structure that accompanies the subsurface thermal front described in the previous section. We call this structure the subsurface salinity front for simplicity.

The vertical distribution of salinity gradients along a quasi-zonal section roughly at 26°S and a meridional section at 105°E is shown in Figure 6c (same sections as exhibited in Figure 5). Along the 26°S section, the salinity gradients are negative between the surface and 150 m, and positive between 200 and 400 m ($26 \leq \sigma_\theta \leq 26.6$). Notice that the positive gradients are stronger east of 65°E, reaching 1.2×10^{-1} g kg^{-1}/100 km. A comparison between the vertical distribution of salinity and temperature gradients (Figures 6 and 5, respectively) shows that the subsurface salinity front ($26 \leq \sigma_\theta \leq 26.5$) is thinner than the thermal one ($24(25) \leq \sigma_\theta \leq 26.5$).

Along the 105°E section (Figure 6c, right), the strongest positive salinity gradients (0.8×10^{-1}g kg^{-1}/100 km) are found in the southern SICC region, and confined to 150–300 m depth. North of 28°S, the

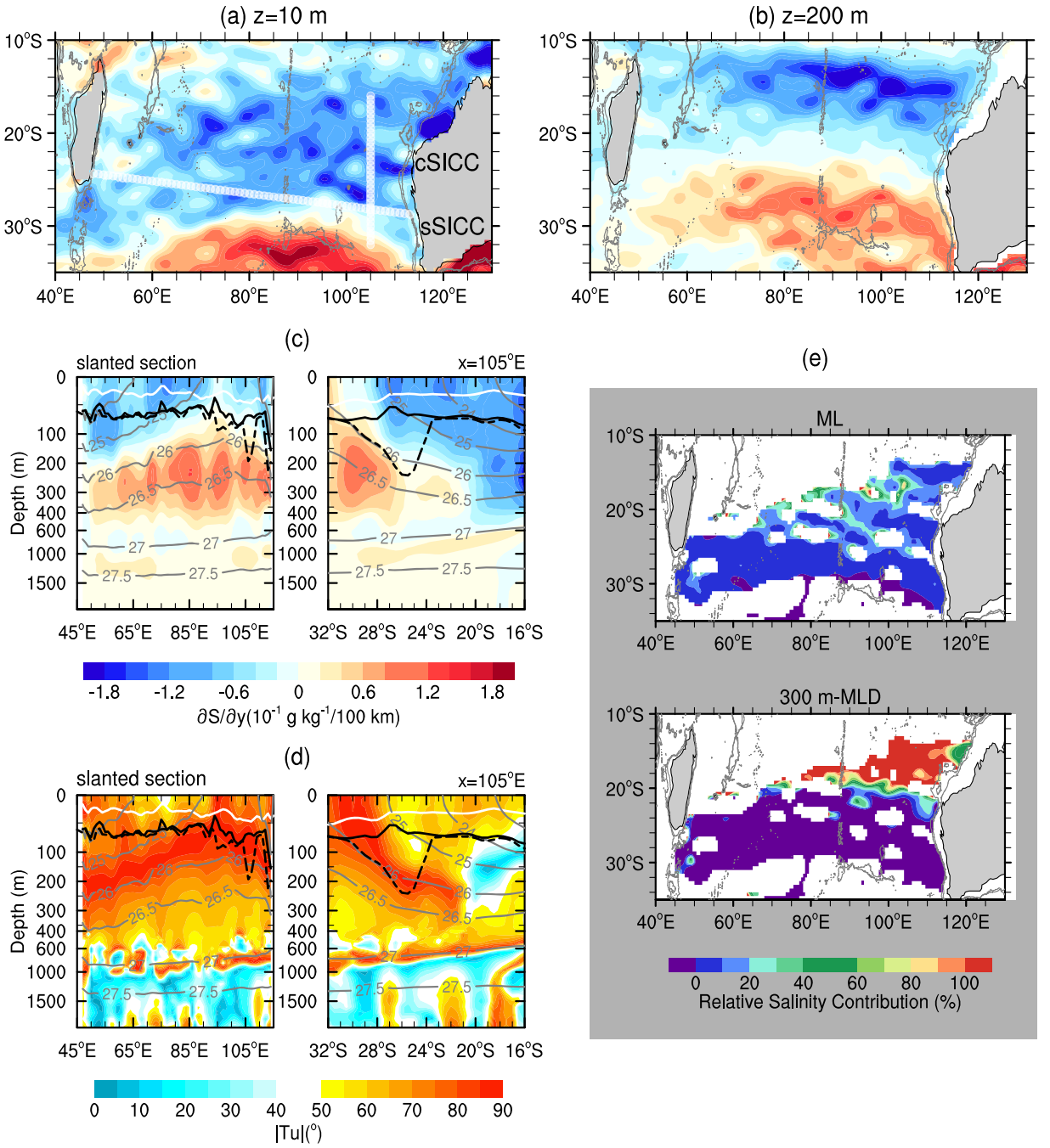

Figure 6. Annual mean meridional gradient of salinity ($\partial S/\partial y$) from CARS09 at (a) 10 m and (b) 200 m. White lines show the position of the sections plotted in (c, d). In Figure 6c, $\partial S/\partial y$ along the slanted section (left, no average) and along 105°E (right, averaged between 102.5° and 107.5°E). In Figure 6d, same sections but for meridional Turner angles $|Tu|$ (no averages). Contours in Figures 6c and 6d are (i) the σ_θ (gray), (ii) the mixed layer depth (white), (iii) the depth of the maximum $\partial\theta/\partial z$ (dashed black), and (iv) the depth of maximum Brunt-Väisala frequency (black). The latter contours have been smoothed with a three-point running mean in longitude (≈1.5°) to reduce the noise. (e) Relative salinity contribution (%) to the annual mean surface eastward currents (see text for details). Gray contours in the maps are the 2000 m and 3000 m isobaths from Smith-Sandwell 2 min bathymetry. cSICC (sSICC) stands for the central (southern) SICC branch.

vertical distribution is characterized by an upper layer with strong negative salinity gradients ($\leq -0.8\times10^{-1}$g kg^{-1}/100 km) sitting above a layer with weak positive salinity gradients ($\leq 0.2\times10^{-1}$g kg^{-1}/100 km). The thickness of the negative salinity gradient layer increases equatorward from 0–150 m at 26°S to 0–400 m, at 16°S (σ_θ=27).

To address the hypothesis raised by *Palastanga et al*. [2007] and *Siedler et al*. [2006] that the salinity effects dominate the density in the SICC region, both meridional Turner angles (T_u) and salinity/temperature contributions to SICC zonal velocities have been computed (see section 3). The interpretation of T_u is straightforward: $|T_u| \ll 45^\circ$ means that the salinity gradients dominate the density variations, $|T_u| \gg 45^\circ$ means that temperature dominates, and a density compensation occurs when $|T_u| = 45^\circ$ [*Tippins and Tomczak*, 2003].

Contrary to the suggestion of *Palastanga et al*. [2007] and *Siedler et al*. [2006], the vertical distribution of meridional Turner angles along the 26°S quasi-zonal section shows that temperature dominates the meridional density gradients, from the surface to 1000 m (Figure 6d, left). Only below $\sigma_\theta = 27$ (depths > 1000 m) does salinity dominate the meridional density gradients (blue colors in Figure 6d).

A meridional section of T_u at 105°E also shows that temperature dominates the meridional density gradients between 32° and 22°S, from the surface to $\sigma_\theta = 27$ (depths around 700–1000 m), with salinity dominating the density gradients only below this level (Figure 6d, right). North of 22°S, salinity dominates density gradients at two depth ranges: between 50 and 300 m and below 600 m ($\sigma_\theta = 27$).

The relative contributions from mixed layer and subsurface salinity gradients for total *u* (including temperature) at the surface were determined in a similar way as done for the temperature gradients (see section 4.2). The vertical shear $\partial u_S/\partial z$ was integrated from the MLD upward to the surface to give the mixed layer salinity contribution (u_{Sml}) and from 300 m upward to the MLD to give the subsurface salinity contribution (u_{Stherm}) (Figure 6e). In the mixed layer, salinity gradients contribute between 5 and 20% to eastward shear. The uncertainty associated with the split of the contributions, which depend on the local thickness of the mixed layer, has been also evaluated using the deeper MIMOC MLD as reference. The root-mean square of the difference between the mixed layer contribution using MIMOC and using CARS09 (RG) is 4% (3%). In the thermocline level, three different domains can be clearly seen (Figure 6e, bottom): (i) south of 20°S, where salinity gradients do not contribute to eastward shear (purple); (ii) a narrow transition zone in which salinity gradients become progressively more important (from blue to yellow); and (iii) north of 20°S, where the salinity gradients strongly contribute to eastward shear (red, more than 100%).

Three distinct domains are also identified contrasting the total contribution of temperature (r_T) and salinity (r_S) to the total *u* (temperature and salinity) at the surface (Figure 7): (i) south of 22°S where the meridional gradients of temperature dominate the eastward shear; (ii) a transition zone between 22°S and 18°S, where temperature gradually becomes less important; and (iii) a salinity-dominated zone north of 18°S, where the EGC flows. Notice that in these maps, the transition zone is slightly broader than in the salinity contribution maps separated by layers of Figure 6e.

Thus, it is clear that the eastward shear of the sSICC is dominated by meridional temperature gradients, while the salinity gradients act to reduce it ($r_S < 0$) since they contribute to westward shear. Although in the mixed layer, the gradients of salinity are negative, the net salinity effect, i.e., integrating all layers from 1950 dbar upward to the surface, is westward due to the strong positive gradients between 200 and 400 m (Figure 6c). In the northern and central SICC, both temperature and salinity gradients contribute to eastward shear although temperature is the major contributor in general (60–90%). Hence, our analysis reinforces the idea that the subtropical SICC, for which the eastward shear arises from thermal meridional gradients, is different from the tropical EGC, for which eastward shear is dominated by meridional salinity gradients [see e.g., *Menezes et al*., 2013].

4.5. Seasonal Variability

The subsurface thermal front associated with the sSICC is persistent throughout the year and is a robust feature in the three atlases analyzed here. No substantial seasonal variations are observed e.g., in the subsurface temperature gradients at 200 m (Figure 8a). At this depth, the sSICC front has monthly temperature gradients around 1°C/100 km, which are of the same order as the annual mean gradients (Figure 5b). The monthly subsurface front exhibits a meandering pattern, clearly seen in MIMOC (not shown), a characteristic also present in the annual mean fields.

Monthly temperature gradients, averaged over a region that encompasses most of the sSICC front (rectangle in Figure 8a), is shown in Figure 8b for three different depths (10 m, 150 m, and 200 m). Note that the subsurface front (e.g., 150 m and 200 m) is present throughout the year, with averaged gradients around 0.75°C/100 km. Although the subsurface front has no substantial seasonal variations, it is slightly weaker

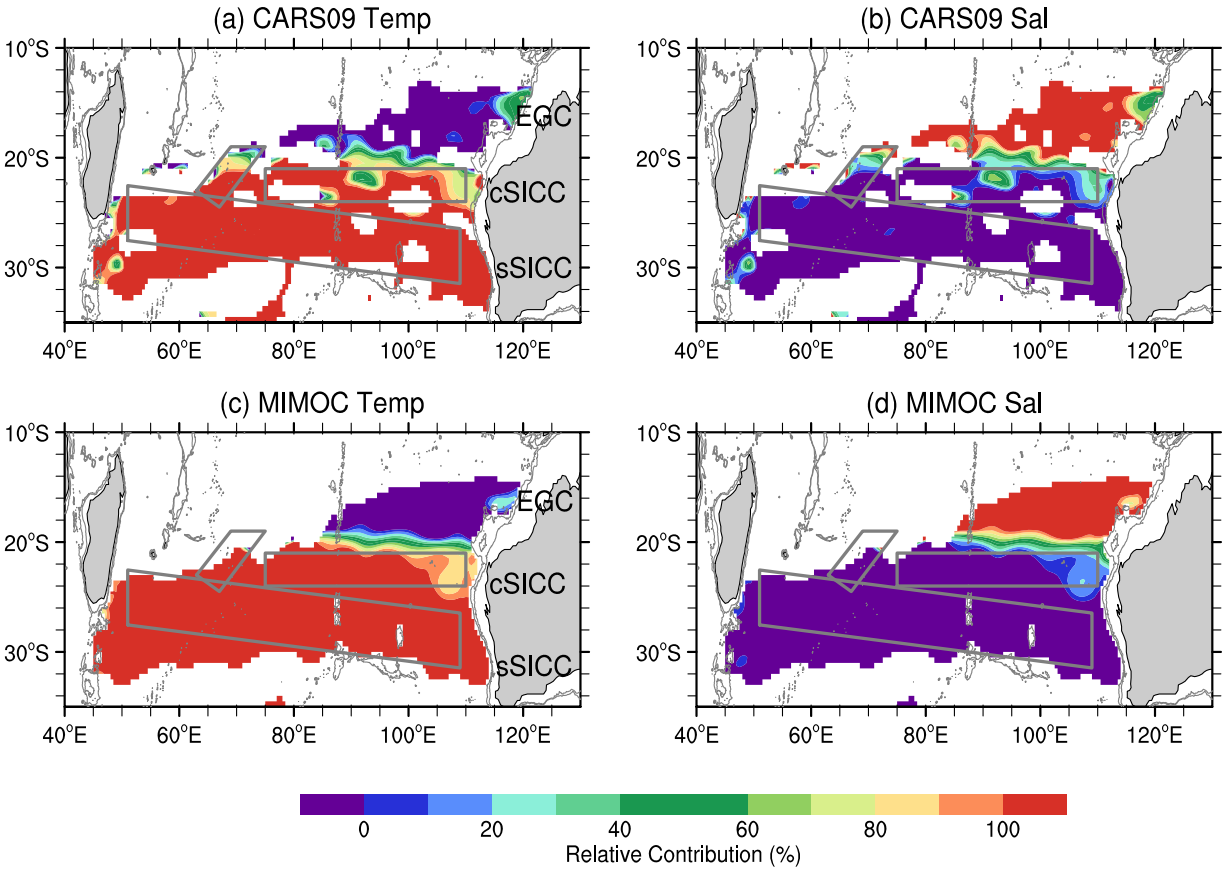

Figure 7. Relative thermal and salinity contributions (%) (including mixed layer and thermocline) to the annual mean surface eastward currents from CARS09 and MIMOC. White line shows the axis of the subsurface thermal front associated with the sSICC. Gray contours are the 2000 m and 3000 m isobaths from Smith-Sandwell 2 min bathymetry. cSICC (sSICC) stands for the central (southern) SICC branch. The boxes indicate the areas corresponding to the SICC branches. The sSICC is within the southern rectangle with a slightly poleward slant, the cSICC is within the central zonal one, and the nSICC appears in the polygon with the marked equatorward slant centered near 70E.

during the austral autumn-winter (Figure 8b). In contrast, the mixed layer gradients have a strong seasonality, with the highest gradients ($\approx 0.6^{\circ}$C/100 km) found during the austral winter-spring seasons (July–September). The highest gradients are associated with the northward shift of the North Subtropical Front [*Lan et al.*, 2012; *Belkin and Gordon*, 1996]. The seasonal north-south shift of the North Subtropical Front is very clear in the monthly $\partial\theta/\partial y$ maps from the mixed layer in the three atlases analyzed here (not shown). The mixed layer temperature gradients are also strongest in the austral winter-spring in the eastern basin north of 24°S (not shown).

Using the same procedure as used for the annual mean fields (see section 4.2), we estimated the monthly geostrophic zonal velocities at the surface due to the shear from temperature gradients of the mixed layer (u_{Tml}) and of the subsurface layer u_{Ttherm} (MLD-300 m). For this computation, the monthly MLD fields have been used, so the $u_{Tml}(u_{Ttherm})$ depends on the seasonal variations of the mixed layer thickness. We also calculated the monthly zonal geostrophic velocity u at the surface relative to 1950 dbar from the density fields.

Monthly time series of u_{Tml}, u_{Ttherm}, u, and MLD from CARS09 averaged over five different regions (A–E) were constructed (Figure 9). Similar figures have been produced for RG and MIMOC but are omitted here for brevity. Differences among the three atlases are discussed when appropriate. The five regions have dimension of 3° (lat) × 15° (lon) and were chosen to describe the three SICC branches: region A (23°–20°S; 65°–80°E) relates to the nSICC; regions B (27°–24°S; 50°–65°E), C (29°–26°S; 70°–85°E), and D (28.5°–25.5°S; 95°–110°E) relate to the sSICC; and region E (23°–20°S; 95°–110°E) relates to the cSICC. The three SICC branches are present all year round with surface zonal velocities (referenced to 1950 dbar) between 3 and

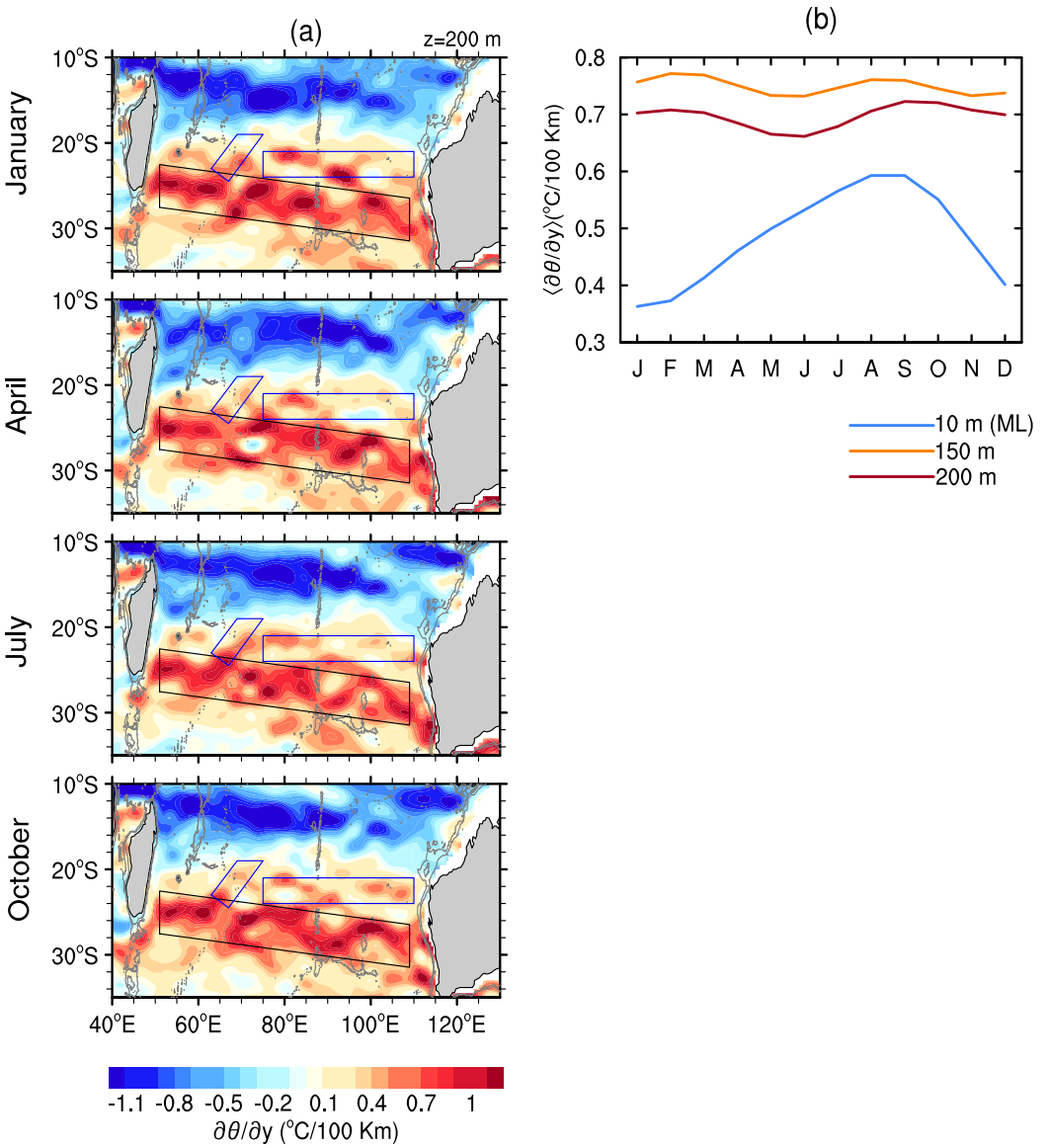

Figure 8. Seasonal cycle of meridional gradients of potential temperature ($\partial\theta/\partial y$) from CARS09. (a) At 200 m. Note that the thermal front around 26°S is present throughout the year. (b) In the sSICC region at 10 m, 100 m, and 150 m depth (averaged in the black box region shown in Figure 8a). Gray contours are the 2000 m and 3000 m isobaths from Smith-Sandwell 2 min bathymetry. The boxes indicate the areas corresponding to the SICC branches. The sSICC is within the southern rectangle with a slightly poleward slant and the cSICC is within the central zonal rectangle. The polygon with the marked equatorward slant centered near 70E only indicates the region where the nSICC is strongest.

10 cm/s, the nSICC being the weakest one (maximum of 5 cm/s). CARS09 and RG have average eastward velocities generally of the same order, while MIMOC presents the weakest currents in all five regions probably due to the smoothing applied in the MIMOC construction. Differences between CARS09 and RG are found only in the region B (sSICC, western basin) and E (cSICC) where RG has eastward velocities up to 2 cm/s greater than CARS09 (not shown). These differences are likely to be a consequence of decadal variations sampled over the longer period covered in the CARS09 atlas. However, for each region, the seasonal cycle is consistent among the three atlases.

Except for region A (nSICC), the subsurface thermal front contributes most for the eastward shear of the SICC throughout the year. Compare the time series from u (blue curves) with that from u_{Ttherm} (red curves) in Figure 9. In region A (nSICC), the mixed layer and subsurface front contributions are of same order, with u_{Tml} being slightly larger than u_{Ttherm} in the austral winter (June–August) when the MLD reaches 60–90 m in

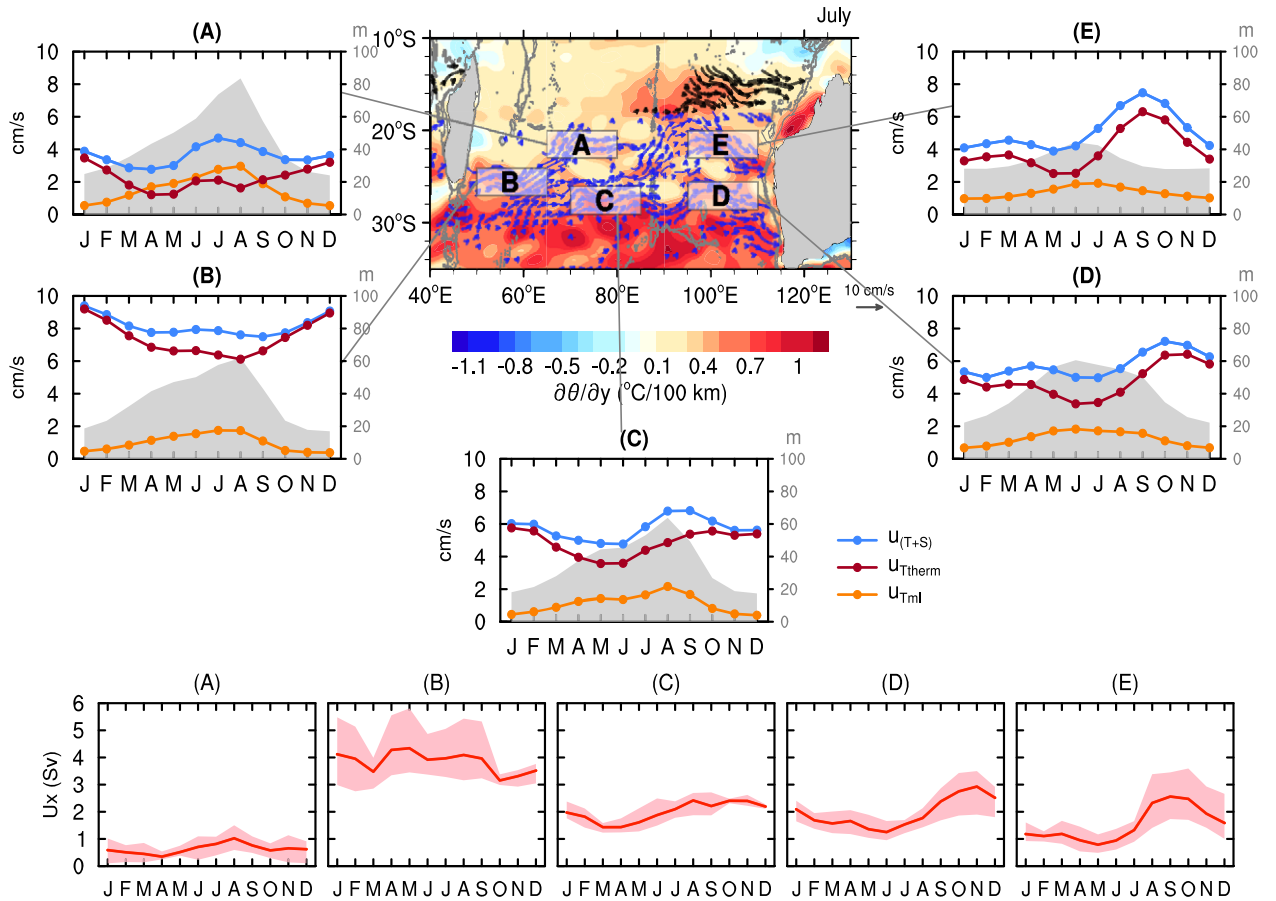

Figure 9. Seasonal variability of the surface geostrophic zonal velocities and mixed layer depth (MLD) from CARS09, averaged in five regions (A–E, see text for details). Blue time series are the total zonal velocity ref. to 1950 dbar computed from the density fields. Red and orange time series show the shear contribution (temperature only) from the subsurface layer (300 m-MLD) and mixed layer, respectively. Gray shadings are the MLD (values are on the right *y*-axis). Map shows the surface potential temperature gradients ($\partial\theta/\partial y$) in July and surface geostrophic circulation (vectors). Vectors are only plotted for eastward currents with intensities greater than 1.5 cm/s. Gray contours in the map are the 2000 m and 3000 m isobaths from Smith-Sandwell 2 min bathymetry. (bottom) The average eastward geostrophic volume transports (U_x) 0/300 m in Sverdrups (1 Sv $\equiv 10^6 m^3/s$) for each region A–E. Red curves are the mean between CARS, RG, and MIMOC and pink shadings are respective minimum/maximum U_x.

this region (the deepest mixed layer in the regions analyzed here). Note that in the austral winter, the mixed layer $\partial\theta/\partial y$ is stronger (see e.g., Figure 8b) and the MLD are deeper (gray shadings in Figure 9). Thus, in all regions during the austral winter, the mixed layer contributions increase and consequently the subsurface contributions decrease.

Although mixed layer contributions during the austral winter are not essential for the SICC existence (most of the vertical shear originates from the MLD-300 m layer in regions B–E), they are important for the SICC strength in the eastern basin during the winter, especially for the cSICC (region E). In the cSICC, the u_{Tml} and u_{Ttherm} are of same order in July, even though in this region the MLD does not present a strong seasonal variability (MLD between 30 and 40 m all year round).

Additionally, we calculated the monthly geostrophic zonal velocity at the surface due to the shear from salinity gradients of the mixed layer (u_{Sml}) and of the subsurface layer (u_{Stherm}) for the five regions shown in Figure 9. Salinity only contributes to eastward shear in the mixed layer. These contributions are negligible (less than 0.5 cm/s), except for the weak nSICC, where u_{Sml} reaches a maximum of 1 cm/s during the winter season (not shown).

The monthly mean eastward volume transports $U_x(x,t)$ between 0 and 300 m have been estimated separately for each region A–E in a manner similar to that for the annual mean (see section 3.4), except that the *y*-limit of integration used for the seasonal fields are the latitude limits of each region (see Figure 9). Then, the eastward transports were averaged in longitude bins for each region. Figure 9 (bottom) shows the

monthly mean eastward transports averaged between the three atlases (red curves) and respective minimum/maximum transports (pink shadings). The lowest transports are found in region A (nSICC), with maximum transport of about 1 Sv (August). Region B, where the southern SICC begins as a strong and well-organized jet, has the highest transport with mean value of 4 Sv all year round but it can reach ≈6 Sv (pink shading). In regions C–E, the transports vary seasonally between ≈1 Sv (April–Jun) to 3 Sv (August–October).

4.6. Hydrographic Data: Subsurface Thermal Front Snapshots

The subsurface thermal front described in the previous sections is also identified in the six hydrographic meridional sections analyzed here. These snapshots corroborate the idea that this front is a permanent feature of the South Indian Ocean. In Figure 10, we show vertical sections of potential temperature (colors and gray contours) along 55°E, 80°E, 95°E, and 105°E from CTD data (left) and climatological values from the RG atlas (right). Note that RG is based only on Argo data, hence none of the CTD data shown on the left side are used in its construction. CARS09 and MIMOC present similar distributions (not shown) but they are not truly independent data sets since CTD data from WOCE cruises have been used in their construction. Contours superimposed on the potential temperature are σ_θ (black) and meridional temperature gradients (white).

Broadly speaking, the subsurface front positions (white contours) are found in similar latitudes as the climatological fronts, although climatological gradients are weaker than the synoptic sections, as expected. Differences between the synoptic and climatological sections are also observed in Figure 10. These differences can be due to eddies, planetary waves, internal waves, tides, and other transient phenomena that are measured in the synoptic sections but are not present in the climatologies (average). Particularly, the region where the SICC flows is characterized by relatively high eddy kinetic energy (EKE) and prominence of planetary waves and westward-propagating eddies in several time scales [e.g., *Siedler et al*., 2006; *Palastanga et al*., 2007; *Jia et al*., 2011]. Hence, all the synoptic sections analyzed here are noisier than the climatological ones. For example, at 95°E, the fronts are displaced from their climatological positions in both 1995 and 2007 cruises, possibly due to the presence of eddies. *Palastanga et al*. [2007] analyzed both hydrographic and LADCP (Lowered Acoustic Doppler Current Profiler) data at 95°E (1995) and found indications of an anticyclonic eddy around 24°S, where the temperature gradients are strongest in Figure 10. At 105°E, in both 2012 and 2013 hydrographic sections, two maxima in meridional temperature gradients can be identified: one around 29°S–30°S, which is also observed in the climatological sections, and another around 26°S–27°S. In both synoptic sections at 105°E, the absolute geostrophic circulations derived from altimetry data for the same period show the presence of a strong eddy between 25°S and 28°S (anticyclonic in 2012 and cyclonic in 2013), where the second maximum is found in each section (not shown). The eddy signature is also found in concurrent LADCP and shipboard ADCP data, being also clear in tracer data such as oxygen (not shown).

Despite the differences between the synoptic and climatological sections, the fronts are mostly confined above 400 m depth in the hydrographic data and are associated with the poleward shoaling of the upper thermocline. This broadly agrees with the previous descriptions based on the climatological atlases, in which the climatological front is relatively shallow and located in the thermocline level. The isotherms (gray contours) follow the isopycnals, indicating that temperature largely controls the density definition. Analysis of the meridional Turner angles (not shown) calculated from the CTD data reveals that temperature gradients control density gradients in the region south of 23°S for all sections. In this region, salinity gradients only dominate density gradients below 900 m depth ($\sigma_\theta \leq 27.2$) on the 105°E section. The salinity dominance on density at intermediate depths south of 26°S was also found in the climatological atlases. North of 23°S, the salinity controls density in the upper 200 m and below 800 m depth at the 80°E and 95°E sections. At the western basin (55°E), temperature dominates density along the section, with salinity being of minor importance. These results agree with the analyses of the climatological atlases, in which we found salinity was only important for eastward shear in the eastern basin north of 22°S.

5. The SICC and Two PV Paradigms

Kobashi and Kubokawa [2012] have called attention in their conclusion section to the fact that the SICC flows along the equatorward flank of two low subsurface PV regions as expected for a STCC-like current. These regions would correspond to the Indian Ocean Subtropical Mode Water (IOSTMW) (25.8–26.7 σ_θ) in the western basin, and to the (denser) south-east Sub-Antarctic Mode Water (SAMW) (26.5–26.9 σ_θ) in the eastern basin [e.g., *Tsubouchi et al*., 2010; *McCarthy and Talley*, 1999, and references therein].

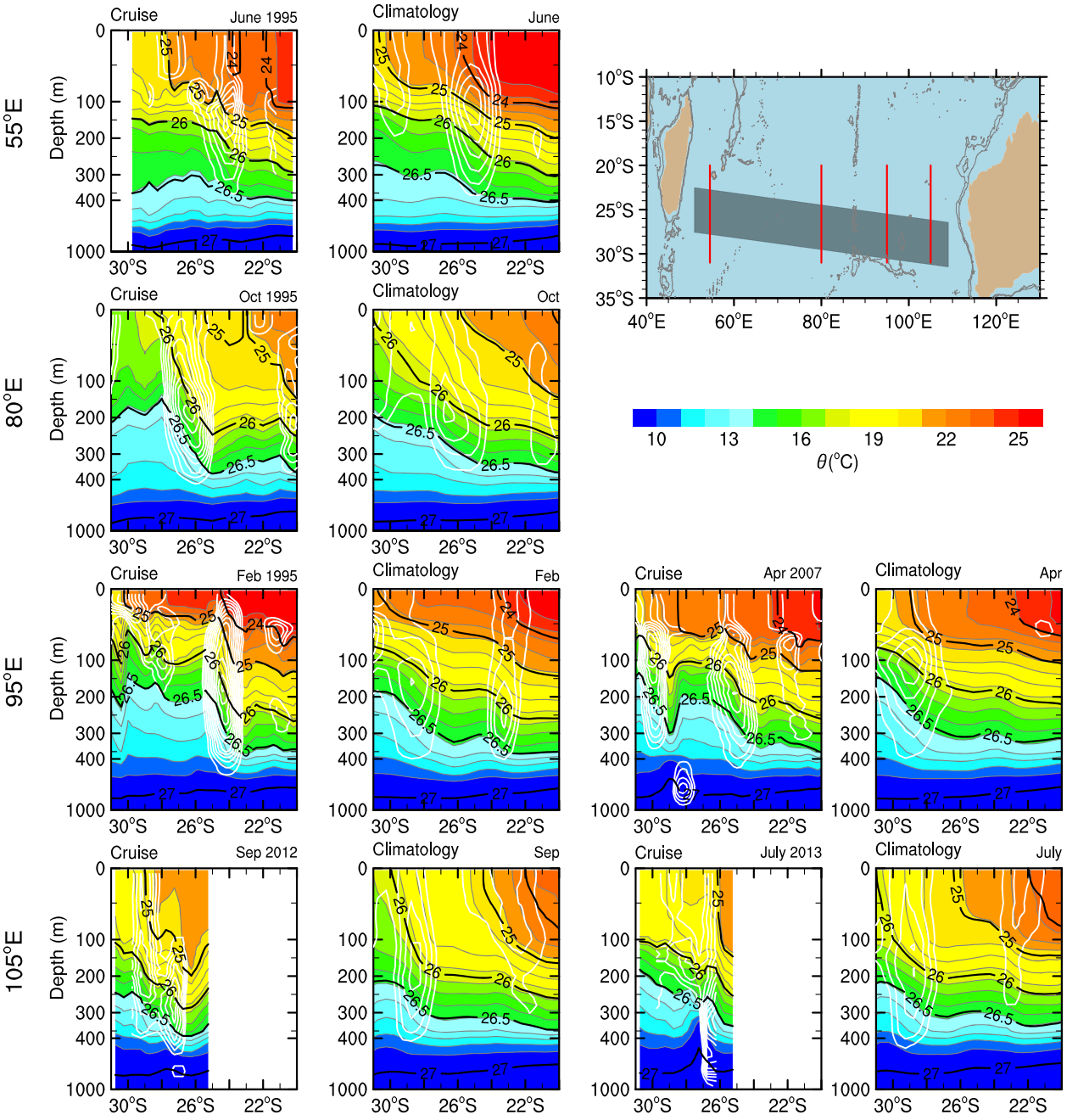

Figure 10. Vertical sections of potential temperature (θ) from six (left) hydrographic cruises and (right) climatological values from RG atlas along 55°E, 80°E, 95°E, 105° (see map for positions). Contours are gray for isotherms every 1°C; black for isopycnals σ_θ=24, 25, 26 and 26.5; and white for meridional gradients of potential temperature between 0.5 and 2.9°C/100 km, every 0.2°C, marking the position of the thermal front (see text for details). In the map, the shading box is the same box as shown in Figure 8 and indicates the position of the annual mean subsurface front, and gray contours are the 2000 m and 3000 m isobaths from Smith-Sandwell 2 min bathymetry.

In general terms, the formation of a thick low-PV layer (a mode water) on the poleward side of the STCC front pushes the upper pycnocline upward, forming a meridional density front at the upper thermocline level and a shallow eastward current by the thermal wind relation [*Aoki et al.*, 2002; *Kobashi et al.*, 2006; *Kobashi and Kubokawa*, 2012, and references therein]. To facilitate the reading here, Figure 11 (top) presents a schematic that illustrates this mechanism [as done in *Kobashi et al.*, 2006], but adapted for the southern hemisphere ($f < 0, \partial\rho/\partial y < 0$).

In the modern STCC paradigm, the frontal strength is tightly related to the meridional gradient of PV, vertically integrated in the range between the upper and lower pycnoclines [*Kobashi et al.*, 2006, section 4]. In

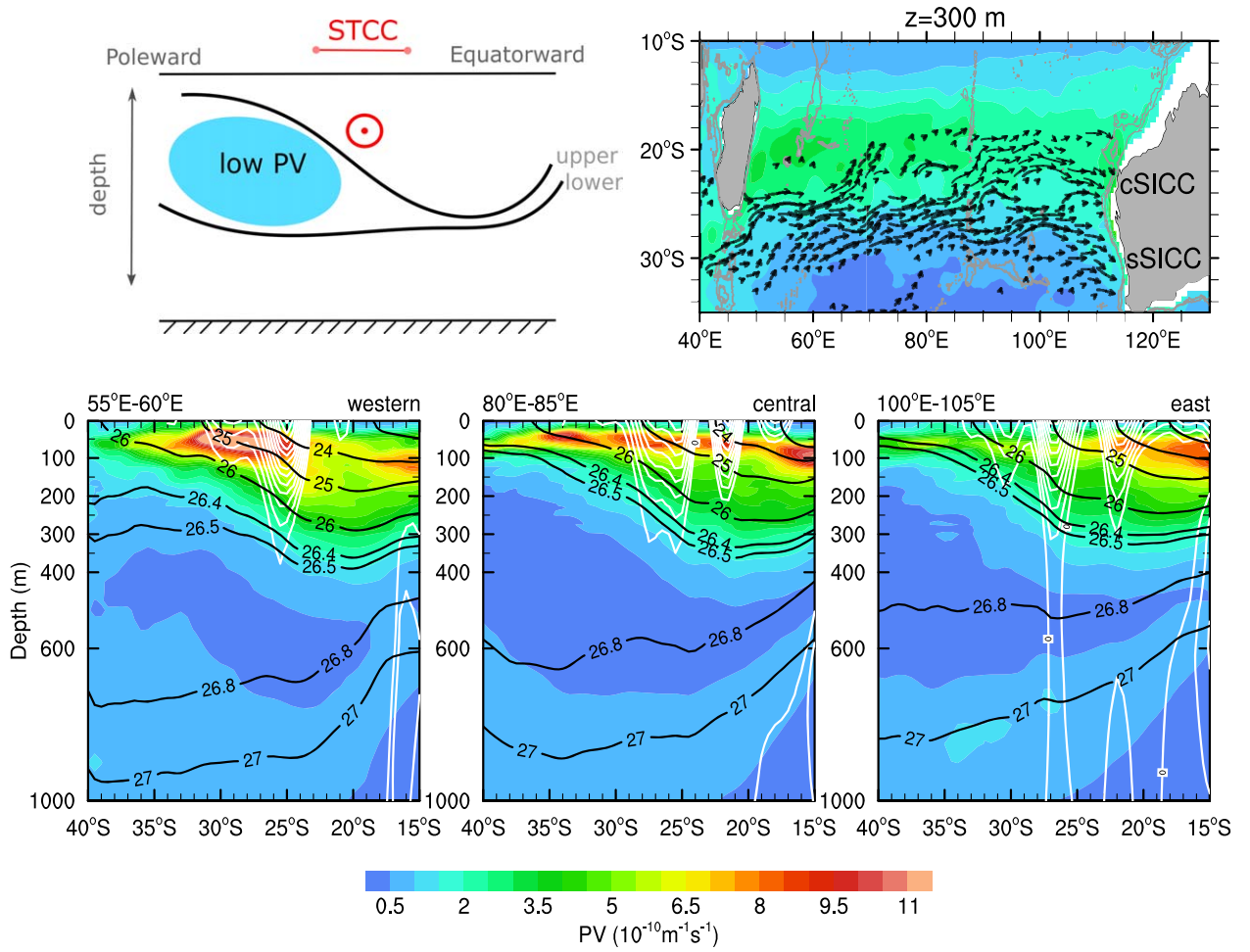

Figure 11. (Ertel) Potential vorticity in the SICC from the annual mean CARS09 atlas. (top) Schematic showing the STCC-paradigm from *Kobashi et al.* [2006] adapted for the Southern Hemisphere (upper and lower refer to the pycnocline), and the *PV* at 300 m (map). In the map, vectors show the SICC at the surface and gray contours the 2000 m and 3000 m isobaths from Smith-Sandwell 2 min bathymetry. (bottom) Vertical sections of *PV* (color), density (black lines), and eastward zonal velocities (white) averaged in three regions: (left) between 55°E and 60°E, (middle) 80°E and 85°E, and (right) 100°E and 105°E. SICC (sSICC) stands for the central (southern) SICC branch.

the present section, we investigate whether the SICC and its branches can be explained by this STCC PV paradigm. To this end, we compute the annual mean (Ertel) PV fields obtained from CARS09 as $PV=(f/\rho_0)(\partial\sigma_\theta/\partial z)$, also assuming that the relative vorticity is negligible as done by *Aoki et al.* [2002] and *Kobashi et al.* [2006]. In this section, all gradients have been estimated using centered finite differences.

We also use the diagnostic relation between the density front and the meridional PV gradients derived by *Kobashi et al.* [2006], which we briefly repeat here to make the paper self-consistent. Recall that potential vorticity is actually a class of quantities, not a specific variable [see *Muller*, 1995, for a comprehensive review on the subject]. Throughout the paper, we refer to the potential vorticity under the quasi-geostrophic theory (QG) as q and the (Ertel) potential vorticity as PV (remember that they have different dimensions), although in *Kobashi et al.* [2006] no such distinction is pointed out, which may cause some confusion when one tries to reproduce their analysis. Under QG dynamics, the potential vorticity is given by [e.g., *Vallis*, 2006]

$$q=f+\frac{\partial}{\partial z}\left(\frac{f^2}{N^2}\left(\frac{\partial\psi}{\partial z}\right)\right) \tag{5}$$

where the relative vorticity is neglected, f is the Coriolis parameter, N^2 is the square of the Brunt-Väisala frequency, and ψ is the geostrophic stream function. Taking the meridional derivative of equation (5), noting that in the integrand $\partial\psi/\partial y=-u$, and using the thermal wind relation, by simple algebra we get the

Kobashi et al. [2006] formula for $\partial\rho/\partial y$, which represents a diagnostic relationship between the frontal strength and the integrated meridional gradient of q underneath the front:

$$\frac{\partial\rho}{\partial y}=\frac{\rho_0 N^2}{gf}\int_{z_0}^{z}\left(\beta-\frac{\partial q}{\partial y}\right)\,dz'+\frac{\partial\rho(z_0)}{\partial y} \tag{6}$$

As *Kobashi and Kubokawa* [2012] have already noticed, the SICC (in fact its southern branch) flows on the equatorward flank of a low-*PV* pool ($<1\times10^{-10}\mathrm{m}^{-1}\mathrm{s}^{-1}$), which is located at depths below the sSICC thermal front ($\geq$ 300 m). In density coordinates, this pool is not zonally continuous in a specific σ_θ, as shown by *Kobashi and Kubokawa* [2012], Figure 19, because the IOSTMW in the western basin is slightly lighter than the SAMW. In z coordinates, however, the low-*PV* pool located poleward of the sSICC is zonally continuous because the isopycnals are slighter deeper in the western basin than in the eastern. For example, the *PV* distribution at 300 m, just below the front and roughly equivalent to the σ_θ maps from *Kobashi and Kubokawa* [2012], is shown in Figure 11 (map) overlaid by the SICC at the surface. While a poleward low-*PV* pool is clearly identified for the sSICC, a similar pool is not observed either for the central or for northern SICC branches. The *PV* is relatively higher in those regions at 300 m ($>2\times10^{-10}\mathrm{m}^{-1}\mathrm{s}^{-1}$). We have examined in detail the *PV* maps from several depths (300–1500 m) and did not identify a characteristic low-*PV* pool just poleward of the nSICC or the cSICC.

To investigate more closely the relationship between the vertical structures of *PV* and density, and the STCC paradigm used by the above-cited authors, three average meridional sections of *PV*, σ_θ, and u were constructed: (i) between 55°E and 60°E, where the SICC is a strong and well-organized jet; (ii) 80°E–85°E, where three SICC branches appear; (iii) 100°E–105°E where the sSICC and cSICC are particularly distinct (Figure 11, bottom). In general, the *PV* distribution in the three sections resembles the STCC schematic diagram of *Kobashi et al*. [2006] (adapted here for the Southern Hemisphere) with a wedge-like low-*PV* pool between the upper and lower pycnoclines. The low-*PV* ($<0.5\times10^{-10}\mathrm{m}^{-1}\mathrm{s}^{-1}$), roughly between 300 m and 600 m, seems to cause the upper pycnocline ($26.4\sigma_\theta-26.5\sigma_\theta$) to shoal around 25°S–30°S where the sSICC flows. A careful analysis of the sections in the central and eastern basins, however, does not give an observational support to the idea that a low-*PV* pool is causing the lifting of the upper pycnoline in the nSICC and the cSICC regions. Instead, in these regions, we find undulations on the *PV* contours, like plateaus, mainly in the cSICC region between 100 and 450 m depth (central and east *PV* vertical sections).

The QG diagnostic relation derived by *Kobashi et al*. [2006] (equation (6)) was then applied to verify whether the southern SICC is associated with the PV distribution below the front. Note that for this computation, the potential vorticity is given by q. The lower limit $z_0=800$ m of integration was chosen to be underneath the low-PV pool as suggested in *Kobashi et al*. [2006]. We have tested other z_0 integration limits between 600 and 1000 m and the results are very similar. The meridional density gradients at 150 m estimated using the QG diagnostic relation are shown in Figure 12a. For a qualitative comparison we have plotted the actual meridional density gradients from CARS09 (Figure 12c), where both the central and southern SICC fronts clearly appear. In general, the QG diagnostic equation retrieves relatively well the position of some fronts (sSICC, EGC, and SEC), although they are weaker than the original ones. The southern SICC front along 26°S and its characteristic meandering is noticeable. A major difference is found in the cSICC region, where the estimated $\partial\rho/\partial y$ is weaker ($0.5–1\times10^{-6}\mathrm{kg\ m}^{-4}$) and mostly confined east of 95°E, while in the CARS09 data it is stronger (up to $2.5\times10^{-6}\mathrm{kg\ m}^{-4}$) and extends from 75 to 80°E to the west of Australia. We have also compared the estimated $\partial\rho/\partial y$ with the actual one for other depths in the range of the SICC fronts (100–300 m) and the most significant differences are always found in the cSICC region (not shown).

The results above suggest that the sSICC front strength is related to the meridional PV gradients in the thermocline level, below the front, similar to a STCC-like current [*Aoki et al*., 2002; *Kobashi et al*., 2006; *Kobashi and Kubokawa*, 2012]. However, the STCC mechanism does not seem to explain the triple jet (or branch) structure of the SICC, especially its well-defined central branch. Based on the estimated $\partial\rho/\partial y$ fields, we have computed the respective zonal currents using the thermal wind equation (Figure 12b). In this case, the reference level of no motion is 800 m. For a qualitative comparison, Figure 12d shows u based on CARS09 data (at the surface using the same reference level). We can see that the QG diagnostic relation gives us the southern SICC, the westward-flowing SEC, the tropical EGC, but not the central branch of the SICC.

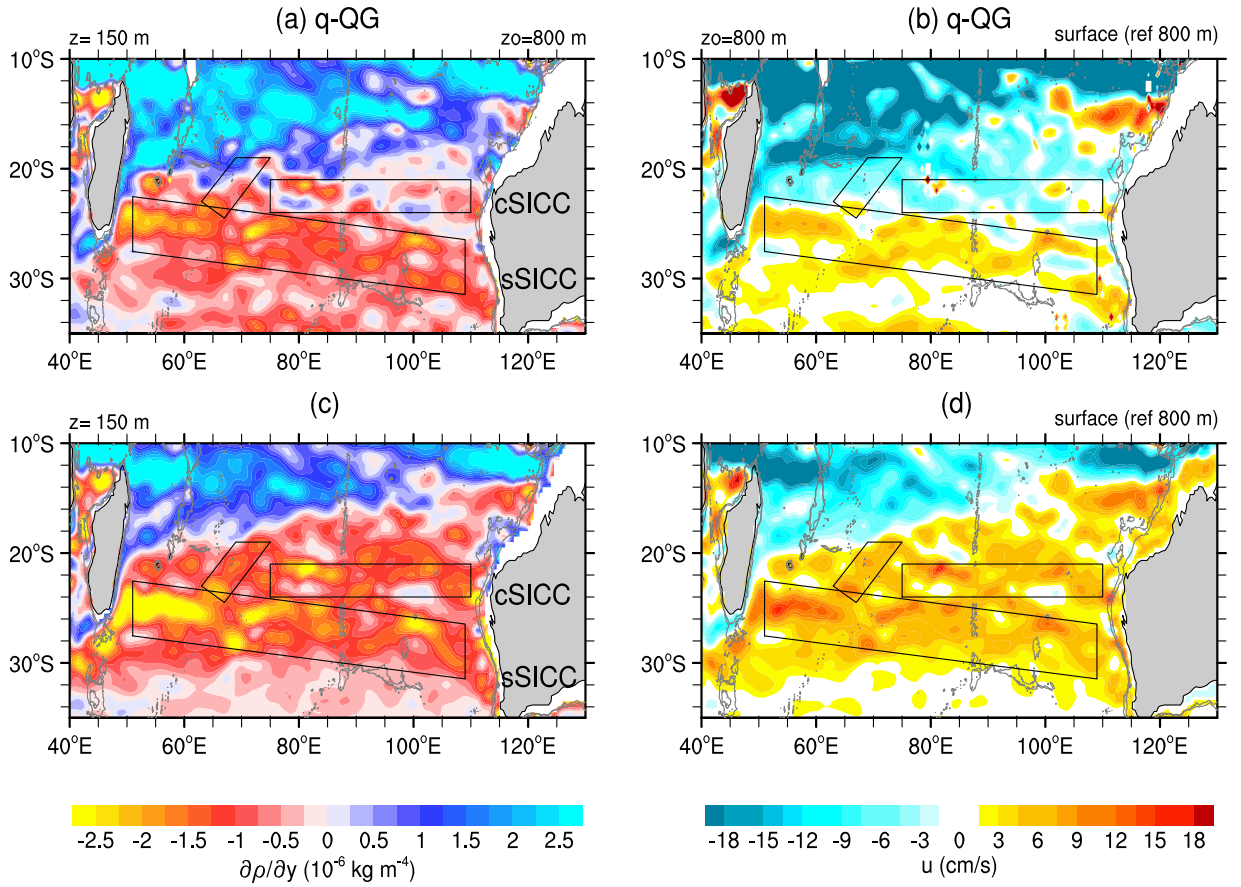

Figure 12. Meridional gradients of density ($\partial\rho/\partial y$) at 150 m estimated using (a) the QG diagnostic equation and (c) from CARS09 data. Geostrophic zonal velocity (u) at surface referenced to 800 m from $\partial\rho/\partial y$ estimated using (b) the QG diagnostic equation and (d) from CARS09 data. z_0 refers to the limit of integration in the QG diagnostic equation (see text for details). The boxes indicate the areas corresponding to the SICC branches. The sSICC is within the southern rectangle with a slightly poleward slant and the cSICC is within the central zonal rectangle. The polygon with the marked equatorward slant centered near 70E only indicates the region where the nSICC is strongest.

Persistent multiple zonal jets are now established as ubiquitous in planetary atmospheres and oceans, hence the SICC pattern observed here should not be an exception. An alternative way to attack the multiple zonal jets problem is to consider the fronts as discontinuities in the PV spatial distribution. Following this train of thought, it may be worth considering whether the PV staircase paradigm can explain the SICC multiple jet fine structure.

The PV staircase concept may be considered as a new theoretical paradigm that explains the existence of multiple zonal jets by the formation of PV staircases, which result from a complex dynamical self-organization of forced turbulent flows in rotating fluids [*Baldwin et al*., 2007; *Dritschel and McIntyre*, 2008; *Hughes et al*., 2010; *Dritschel*, 2013, and references therein]. In this paradigm, the positive feedback interaction of waves and turbulence are responsible for the generation and maintenance of multiple jet structures, which constitute efficient transport barriers across them. The key to understanding this mechanism is that Rossby-like waves ride on quasi-horizontal gradients of PV, and when they break they produce turbulent mixing of PV, because PV tends to behave like a tracer, being mixed when the fluid becomes turbulent. The mixing homogenizes the PV in localized strip-like regions, which reduces the PV gradients there, and promotes further mixing. Hence, steps are formed in the newly organized meridional PV profile. As a result, the meridional PV profile is characterized by alternating very steep and very weak PV gradients: the so-called PV staircase. By the PV invertibility principle [*Baldwin et al*., 2007; *Dritschel and McIntyre*, 2008; *Dritschel*, 2013], the staircase causes intensified eastward jets located at the latitudes of the steepest PV gradients and weaker westward return flows at the mixed PV steps. Intermingled and interacting with these jets are coherent vortices and eddies, which occupy the homogeneous mixed PV steps and transfer kinetic energy

to the eastward jets. A detailed description of this complex dynamics, however, is beyond the scope of the present paper.

While PV staircases have been illustrated in numerical simulations and some studies indicate that they may occur in the oceans [e.g., *Hughes et al*., 2010; *Chapman and McC. Hogg*, 2013, and references therein], the description of oceanic PV staircases based on observations is still incipient. Since the SICC is embedded in a field of waves and eddy flow patterns [*Morrow and Birol*, 1998; *Birol and Morrow*, 2001, 2003; *Siedler et al*., 2006; *Palastanga et al*., 2007; *Jia et al*., 2011], we briefly examined here whether we can find a PV staircase in the region of occurrence of the SICC branches based on CARS09.

In the depth range of the SICC fronts (100–200 m), the *PV* has an interesting spatial distribution between 20°S and 26°S, with the *PV* contours following an inverted U shape east of 75°E (equatorward up to ≈90°E and then poleward) (Figure 13a).

This feature corresponds to the plateaus observed on the central and eastern vertical *PV* sections of Figure 11. Meridional sections of *PV* at several longitudes in this inverted U feature resemble very much a PV staircase as described in the theoretical studies cited above. To verify whether these staircase-like structures are robust, we averaged the *PV* between 100 and 200 m, in the range of SICC fronts, and between 100°E and 105°E, where the sSICC and cSICC are very distinct (Figure 13b). To make the interpretation easier, we overlaid in Figure 13b the average zonal velocities between the surface and 150 m and 100°E–105°E. We can see that the *PV* meridional profile has a staircase-like form, with a steep gradient where the sSICC flows, a homogenized *PV* between the jets followed by a steep gradient in the cSICC. In the ideal PV staircase paradigm, the spacing of the jets in its simplest form [*Dritschel and McIntyre*, 2008] is given by the scale $L_{jet}=2\left(\frac{L_{Rh}^2(U_{jet})}{L_D}\right)$, where L_D is the Rossby deformation length and $L_{Rh}^2(U_{jet})=U_{jet}/\beta$ is the Rhines scale based on U, β is the meridional gradient of the Coriolis parameter f, and $U_{jet}=(\max u-\min u)$ is the jet velocity. Assuming that $U_{jet}=0.1$ m/s, $\beta=2\times10^{-11}$ (≈25°S) and $L_D=30(40)$ km [*Chelton et al*., 1998], we get a jet spacing of ≈3.3° (2.5°) in latitude. In our figure, the jet spacing is around 4° (100°E), which is roughly consistent with this theoretical estimate. Notice that the spacing between the SICC jets is not constant in longitude and maximum distance is around 100°E (Figure 1a). Further, we did the same average for the QG q to verify whether a staircase-like pattern exists in this linearized PV definition (Figure 13c). Aiming for a better visualization, q was multiplied by -1. We also find a staircase-like profile in q, with a steep q gradient followed by a homogenized q and another q gradient, which corresponds to the SICC branches. Note that, however, the staircase is not well defined in the q as it is in the *PV*. Our conclusion from this brief analysis is that the PV staircase paradigm may well explain the multiple jet fine structure of the SICC, but this conjecture should be investigated in more detail by future research efforts.

6. Summary and Conclusion

We analyzed data from three recently published Argo-based climatological atlases and six hydrographic cruises to determine whether the eastward-flowing SICC is accompanied by permanent subsurface thermal and density fronts, which are features of the STCCs that have been documented for the North Pacific, South Pacific, and North Atlantic oceans. We also investigated the role of salinity in the SICC, conjectured to be important by *Siedler et al*. [2006] and *Palastanga et al*. [2007]. Furthermore, we briefly explored two PV paradigms (STCC and PV staircase) to get some insight about the SICC dynamics, which is currently largely unknown.

We find that the SICC is better described as composed of three main branches in the long-term annual mean geostrophic circulation fields, as seen from several satellite and Argo-based (CARS09 and RG) data sets (e.g., Figure 1). Consistent names were provided for these branches for the first time: the northern, the central, and the southern SICC (Figure 3). Note that these branches are not resolved in the low spatial resolution atlases such as WOA01 or WOA09 [e.g., *Palastanga et al*., 2007; *Jia et al*., 2011; *Kobashi and Kubokawa*, 2012] or even in MIMOC, due to stronger spatial smoothing applied in these products. For example, *Palastanga et al*. [2007] (WOA1) and *Jia et al*. [2011] (WOA9) describe the SICC as a broad and weak eastward flow with maximum velocities of 3–5 cm/s. In contrast, we have shown here that in both CARS09 and RG distinct SICC branches are characterized by zonal velocities greater than 10 cm/s. These intensities are of the same order as the time-averaged SICC obtained from altimetry data [*Siedler et al*., 2006] and high-resolution reanalysis products [*Divakaran and Brassington*, 2011]. *Siedler et al*. [2006] have estimated the

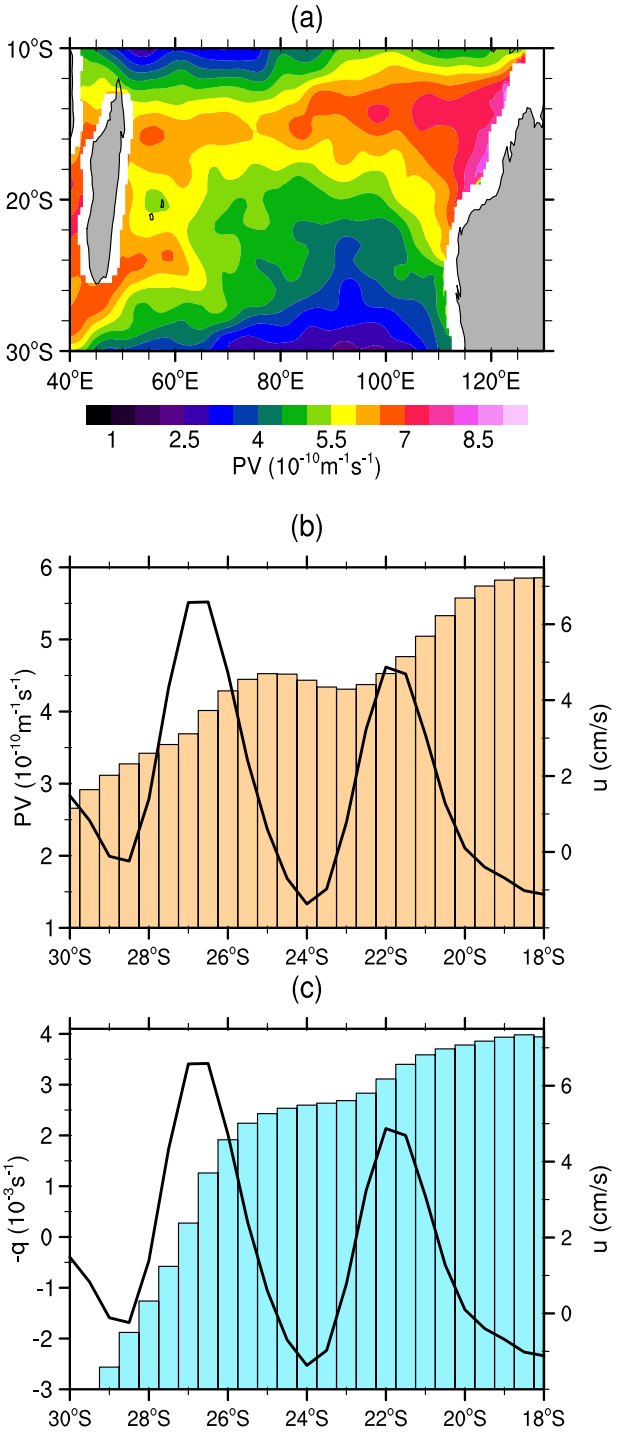

Figure 13. (a) (Ertel) Potential vorticity averaged between 100 and 200 m depth (SICC fronts depth). (b) (Ertel) Potential vorticity (bars, left *y*-axis) and geostrophic zonal velocities *u* (averaged between 100°E and 105°E) and (c) the QG potential vorticity *q* and *u*. In Figures 13b and 13c, the *PV* and *q* are averaged between 100 and 200 m depth and the zonal velocities between surface and 150 m.

zonal volume transports of the SICC near 24°S based on 3 WOCE cruises in 1995 as 10 Sv (54°E), 4 Sv (80°E), and 9 Sv (95°E). Here we estimated the annual mean volume transports of the SICC as being slightly lower than those from *Siedler et al*. [2006], mainly in the western basin. The southern branch crossing the basin around 26°S has annual mean transport of 3–4 Sv, the transport of the central branch (east of 80°E and between 22°S and 24°S) varies from 0.5 Sv (80°E) up to 3–5 Sv (110°E), and the weaker northeastward branch has a transport of less than 1 Sv.

The stronger southern SICC around 26°S is associated with a permanent subsurface thermal front at depth ranges of 100–200 m ($25 \leq \sigma_\theta \leq 26.5$). This subsurface thermal front is present all year round, being slightly weaker during the austral winter. The SICC seasonal cycle is similar to that described by *Palastanga et al*. [2007] and *Jia et al*. [2011], such that the current is stronger in the austral spring-summer ($u \approx 8$–10 cm/s) and weaker in the winter ($u \approx 6$–8 cm/s), although we find some differences in the western, central, and eastern basins. In the western basin, the southern SICC is stronger in December–January while in the eastern basin the maximum flow occurs in October. In the central basin, the maximum strength occurs in August–September. *Jia et al*. [2011] have evaluated the terms of the governing equation for temperature and found that the seasonal changes of $\partial T/\partial y$ in the SICC region are largely controlled by the meridional Ekman and geostrophic flux convergences, and the convergence of the latitudinally dependent surface heat flux forcing. Analyses of these terms indicated that the dynamical forcings are more important than the thermodynamical forcing in modulating the seasonal variations of the vertical shear velocity.

In contrast to the southern SICC, in the central SICC region (east of 75°E–80°E; 22°S–24°E) the thermal front is shallower, around 100 m depth, and confined to densities less than 25 ($\sigma_\theta \leq 25$). Flowing on the southern flank of the slanted northern cell of the subtropical gyre, the shallowest and weakest northern SICC branch has an equatorward orientation. Part of the northern SICC seems to recirculate into the westward-flowing SEC, and part seems to merge with the tropical EGC around 15°S–100°E.

The reason for the existence of a slanted recirculation cell east of Madagascar is still to be determined [*Palastanga et al*., 2007, 2009; *Schott et al*., 2009].

In most of the South Indian Ocean, the salinity gradients are favorable to eastward currents in the mixed layer. However, analyses of the Turner angles and salinity contribution ratios show that salinity is of secondary importance for the southern SICC definition, in agreement with *Jia et al*. [2011] and *Sharma* [1976], and in contrast to the suggestion of *Siedler et al*. [2006] and *Palastanga et al*. [2007].

Although salinity is not significant for the southern SICC definition, we find it is an important feature for the eastern basin circulation, east of the Ninety-east Ridge (≈88°E). In the eastern basin, three distinct domains, which very likely correspond to the biogeographical regions described by *Condie and Dunn* [2006], may be clearly identified: (i) south of 22°S where the meridional gradients of temperature dominate the eastward shear; (ii) a transition zone between 22°S and 18°S, where temperature gradually becomes less important; and (iii) a salinity-dominated zone north of 18°S, coinciding with the EGC flow region [*Menezes et al*., 2013]. Hence, our analysis reinforces the idea that the subtropical SICC, where the eastward shear arises from thermal meridional gradients, is different from the tropical EGC, where the eastward shear is dominated by meridional salinity gradients.

In the South Indian Ocean, identifying the processes leading to the formation of the permanent subsurface thermal fronts associated with the SICC branches is still to be addressed in more detail. In the North Pacific, the existence of the subsurface thermal fronts at thermocline depths associated with the STCC is known to be a result of the interaction of dynamic (wind-driven) and thermodynamic processes at the sea surface, in such a way that either process alone cannot explain the existence of these permanent fronts. This was an important finding by the pioneer studies of *Takeuchi* [1984] and *Cushman-Roisin* [1984].

In the modern STCC paradigm, the frontal strength is tightly related to the meridional gradients of PV, vertically integrated in the range between the upper and the lower pycnoclines [*Kobashi et al*., 2006, and references therein]. *Kobashi and Kubokawa* [2012] have recently suggested that the STCC paradigm would also explain the SICC and hence we have examined this hypothesis. However, it is crucial to keep in mind the differences between the North Pacific and the South Indian Oceans. In the North Pacific, the STCC and its branches extend from the western boundary up to the middle basin around 140°W, while the SICC and its branches extend all the way across the SIO basin. In the eastern basin, the northern SICC branch seems to merge with the tropical EGC, which has no similar counterpart in the North Pacific. The SIO subtropical gyre also has a different structure with two recirculation cells. The recirculation cell centered east of Madagascar, where the SICC begins on its southern flank, is embedded into a north-east slanted MDH ridge. This ridge from Madagascar to the Indonesian Throughflow is a unique feature of the SIO. Furthermore, two mode waters are found poleward of the SICC. One corresponds to the Indian Ocean Subtropical Mode Water (IOSTMW) (25.8–26.7 σ_θ) in the western basin, and the other to the (denser) south-east Sub-Antarctic Mode Water (SAMW) (26.5–26.9 σ_θ) in the eastern basin [e.g., *Tsubouchi et al*., 2010; *McCarthy and Talley*, 1999, and references therein].

Our investigation indicates that the southern SICC front strength is related to the mode waters poleward of the front (IOSTMW and SAMW), which is similar to a STCC-like current [*Aoki et al*., 2002; *Kobashi et al*., 2006; *Kobashi and Kubokawa*, 2012]. However, the STCC mechanism does not seem to explain the triple jet structure of the SICC, especially its well-defined central branch. Since the SICC is embedded in a field of waves and eddy flow patterns [*Morrow and Birol*, 1998; *Birol and Morrow*, 2001, 2003; *Siedler et al*., 2006; *Palastanga et al*., 2007; *Jia et al*., 2011], we briefly examined the possible applicability of the PV staircase paradigm to explain the observed multiple jet SICC structure. Note that different from the North Pacific, in the Indian Ocean the band of high EKE and sea surface height variability extends all the way across the basin between 22°S and 28°S [see e.g., *Jia et al*., 2011, Figure 1].

We find evidence that the PV meridional profile has a staircase-like form, with a steep gradient where the southern sSICC flows, a quasi-homogenized PV zonal strip north of it, followed by a steep gradient at the position of the cSICC. By the PV invertibility principle, the PV staircase causes intensified eastward jets located at the latitudes of the steepest PV gradients and weaker westward return flows at the mixed PV quasi-flat steps. Our brief analysis suggests that the PV staircase dynamics paradigm may explain the multiple jet fine structure of the SICC, and this will be investigated in more detail by future research efforts.

Acknowledgments

We are sincerely grateful to the data providers of CARS09 (CSIRO Marine Laboratories), RG (Scripps Institution of Oceanography), and MIMOC (Pacific Marine Environmental Laboratory) and also to the CLIVAR & Carbon Hydrographic Data Office and the CSIRO Marine Research Centre for the hydrographic data used in this paper. VVM acknowledges use of the Ferret program (NOAA/PMEL) and NCL (http://dx.doi.org/10.5065/D6WD3XH5) for analysis and graphics in this paper. VVM, HEP, CMD, and NLB acknowledge the support of the ARC Discovery Project DP130102088. HEP acknowledges support from NSF grant OCE-091716 PI. VVM is supported by a CSIRO-UTAS QMS Scholarship and an Australian International Postgraduate Research Scholarship (IPRS). The data used in the present study can be obtained directly from the data providers. Last but not least, we are indebted to three anonymous reviewers for their suggestions and challenging questions.

References

Anderssen, R. S., and M. Hegland (1999), For numerical differentiation, dimensionality can be a blessing!, *Math. Comput.*, *68*(227), 1121–1141, doi:10.1090/S0025-5718-99-01033-9.

Aoki, Y., T. Suga, and K. Hanawa (2002), Subsurface subtropical fronts of the North Pacific as inherent boundaries in the ventilated thermocline, *J. Phys. Oceanogr.*, *32*(8), 2299–2311, doi:10.1175/1520-0485(2002)032<2299:SSFOTN>2.0.CO;2.

Baldwin, M. P., P. B. Rhines, H.-P. Huang, and M. E. McIntyre (2007), The jet-stream conundrum, *Science*, *315*(5811), 467–468, doi:10.1126/science.1131375.

Belkin, I. M., and A. L. Gordon (1996), Southern Ocean fronts from the Greenwich meridian to Tasmania, *J. Geophys. Res.*, *101*(C2), 3675–3696, doi:10.1029/95JC02750.

Birol, F., and R. Morrow (2001), Source of the baroclinic waves in the southeast Indian Ocean, *J. Geophys. Res.*, *106*(C5), 9145–9160, doi:10.1029/2000JC900044.

Birol, F., and R. Morrow (2003), Separation of quasi-semiannual Rossby waves from the eastern boundary of the Indian Ocean, *J. Mar. Res.*, *61*(6), 707–723, doi:10.1357/002224003322981110.

Chapman, C. C., and A. McC. Hogg (2013), Jet jumping: Low-frequency variability in the Southern Ocean, *J. Phys. Oceanogr.*, *43*, 990–1003.

Chelton, D. B., R. A. deSzoeke, M. G. Schlax, K. E. Naggar, and N. Siwertz (1998), Geographical variability of the first baroclinic Rossby radius of deformation, *J. Phys. Oceanogr.*, *28*, 433–460.

Condie, S. A., and J. R. Dunn (2006), Seasonal characteristics of the surface mixed layer in the Australasian region: Implications for primary production regimes and biogeography, *Mar. Freshwater Res.*, *57*, 1–22.

Cushman-Roisin, B. (1984), On the maintenance of the subtropical front and its associated countercurrent, *J. Phys. Oceanogr.*, *14*, 1179–1190.

de Boyer Montegut, C., G. Madec, A. S. Fischer, A. Lazar, and D. Iudicone (2004), Mixed layer depth over the global ocean: An examination of profile data and a profile-based climatology, *J. Geophys. Res.*, *109*, C12003, doi:10.1029/2004JC002378.

Divakaran, P., and G. B. Brassington (2011), Arterial ocean circulation of the southeast Indian ocean, *Geophys. Res. Lett.*, *38*, L01802, doi:10.1029/2010GL045574.

Dritschel, D. G. (2013), Waves and turbulence: Their cooperative role in structure formation, *Procedia IUTAM*, *8*, 85–93, doi:10.1016/j.piutam.2013.04.012.

Dritschel, D. G., and M. E. McIntyre (2008), Multiple jets as PV staircases: The Phillips effect and the resilience of eddy-transport barriers, *J. Atmos. Sci.*, *65*(3), 855–874, doi:10.1175/2007JAS2227.1.

Gill, A. E. (1982), *Atmosphere-Ocean Dynamics*, 662 pp., Academic, N. Y.

Graham, R. M., and A. M. De Boer (2013), The dynamical subtropical front, *J. Geophys. Res. Oceans*, *118*, 5676–5685, doi:10.1002/jgrc.20408.

Hughes, C. W., A. F. Thompson, and C. Wilson (2010), Identification of jets and mixing barriers from sea level and vorticity measurements using simple statistics, *Ocean Modell.*, *32*, 44–57, doi:10.1016/j.ocemod.2009.10.004.

IOC, SCOR, and IAPSO (2010), *The International Thermodynamic Equation of Seawater - 2010: Calculation and Use of Thermodynamic Properties*, Intergovernmental Oceanogr. Comm., Manuals and Guides 56, 196 pp., UNESCO.

Jia, F., L. Wu, and B. Qiu (2011), Seasonal modulation of eddy kinetic energy and its formation mechanism in the southeast Indian Ocean, *J. Phys. Oceanogr.*, *41*(4), 657–665, doi:10.1175/2010JPO4436.1.

Johnson, G. C., S. Schmidtko, and J. M. Lyman (2012), Relative contributions of temperature and salinity to seasonal mixed layer density changes and horizontal density gradients, *J. Geophys. Res.*, *117*, C04015, doi:10.1029/2011JC007651.

Kobashi, F., and A. Kubokawa (2012), Review on north Pacific subtropical countercurrents and subtropical fronts: Role of mode waters in ocean circulation and climate, *J. Oceanogr.*, *68*(1), 1–23, doi:10.1007/s10872-011-0083-7.

Kobashi, F., H. Mitsudera, and S.-P. Xie (2006), Three subtropical fronts in the North Pacific: Observational evidence for mode water-induced subsurface frontogenesis, *J. Geophys. Res.*, *111*, C09033, doi:10.1029/2006JC003479.

Lan, K.-W., H. Kawamura, M.-A. Lee, H.-J. Lu, T. Shimada, K. Hosoda, and F. Sakaida (2012), Relationship between albacore (*Thunnus alalunga*) fishing grounds in the Indian ocean and the thermal environment revealed by cloud-free microwave sea surface temperature, *Fish. Res.*, *113*(1), 1–7, doi:10.1016/j.fishres.2011.08.017.

Lutjeharms, J. R. E., and I. J. Ansorge (2001), The Agulhas Return Current, *J. Mar. Syst.*, *30*(1), 115–138, doi:10.1016/S0924-7963(01)00041-0.

McCarthy, M. C., and L. D. Talley (1999), Three-dimensional isoneutral potential vorticity structure in the Indian Ocean, *J. Geophys. Res.*, *104*, 13,251–13,267, doi:10.1029/1999JC900028.

McDougall, T. J., and P. M. Barker (2011), *Getting Started With TEOS-10 and the Gibbs Seawater (GSW) Oceanographic Toolbox*, 28 pp., SCOR/IAPSO Working Group 127, Hobart, Tas, Australia.

McDougall, T. J., D. R. Jackett, F. J. Millero, R. Pawlowicz, and P. M. Barker (2012), A global algorithm for estimating absolute salinity, *Ocean Sci.*, *8*, 1117–1128, doi:10.5194/os-8-1117-2012.

Menezes, V. V., H. E. Phillips, A. Schiller, C. M. Domingues, and N. L. Bindoff (2013), Salinity dominance on the Indian Ocean Eastern Gyral current, *Geophys. Res. Lett.*, *40*, 5716–5721, doi:10.1002/2013GL057887.

Morrow, R., and F. Birol (1998), Variability in the southeast Indian Ocean from altimetry: Forcing mechanisms for the Leeuwin current, *J. Geophys. Res.*, *103*(C9), 18,529–18,544, doi:10.1029/98JC00783.

Muller, P. (1995), Ertel's potential vorticity theorem in physical oceanography, *Rev. Geophys.*, *33*, 67–97, doi:10.1029/94RG03215.

Oke, P. R., D. A. Griffin, A. Schiller, R. J. Matear, R. Fiedler, J. Mansbridge, A. Lenton, M. Cahill, M. A. Chamberlain, and K. Ridgway (2013), Evaluation of a near-global eddy-resolving ocean model, *Geosci. Model Dev.*, *6*, 591–615, doi:10.5194/gmd-6-591-2013.

Palastanga, V., P. J. van Leeuwen, M. W. Schouten, and W. P. M. de Ruijter (2007), Flow structure and variability in the subtropical Indian Ocean: Instability of the South Indian Ocean Countercurrent, *J. Geophys. Res.*, *112*, C01001, doi:10.1029/2005JC003395.

Palastanga, V., H. A. Dijkstra, and W. P. M. de Ruijter (2009), Inertially induced connections between subgyres in the South Indian Ocean, *J. Phys. Oceanogr.*, *39*, 465–471, doi:10.1175/2008JPO3872.1.

Qiu, C., and H. Kawamura (2012), Study on SST front disappearance in the subtropical north Pacific using microwave SSTs, *J. Oceanogr.*, *68*(3), 417–426, doi:10.1007/s10872-012-0106-z.

Ridgway, K. R., J. R. Dunn, and J. L. Wilkin (2002), Ocean interpolation by four-dimensional weighted least squares-application to the waters around Australasia, *J. Atmos. Oceanic Technol.*, *19*(9), 1357–1375.

Roemmich, D., and J. Gilson (2009), The 2004–2008 mean and annual cycle of temperature, salinity, and steric height in the global ocean from the Argo program, *Prog. Oceanogr.*, *82*(2), 81–100, doi:10.1016/j.pocean.2009.03.004.

Rudnick, D. L., and R. Ferrari (1999), Compensation of horizontal temperature and salinity gradients in the ocean mixed layer, *Science*, *283*(5401), 526–529, doi:10.1126/science.283.5401.526.

Rudnick, D. L., and J. P. Martin (2002), On the horizontal density ratio in the upper ocean, *Dyn. Atmos. Oceans*, *36*(1–3), 3–21, doi:10.1016/S0377-0265(02)00022-2.

Schmidtko, S., G. C. Johnson, and J. M. Lyman (2013), MIMOC: A global monthly isopycnal upper-ocean climatology with mixed layers, *J. Geophys. Res. Oceans*, *118*, 1658–1672, doi:10.1002/jgrc.20122.

Schott, F. A., S.-P. Xie, and J. McCreary, J. P. (2009), Indian Ocean circulation and climate variability, *Rev. Geophys.*, *47*, RG1002, doi:10.1029/2007RG000245.

Sharma, G. S. (1976), Water characteristics and current structure at 65E during the southwest monsoon, *J. Oceanogr. Soc. Jpn.*, *32*, 284–296.

Sharma, G. S., A. D. Gouveia, and S. Satyendranath (1978), Incursion of the Pacific ocean water into the Indian ocean, *Proc. Indian Acad. Sci.*, *87*, 29–45.

Shi, S., J. Ribbe, T. Cowan, and W. Cai (2007), A dataset of the wind-driven global ocean circulation for climate research, technical report, paper presented at 14th National Australian Meteorological and Oceanographic Society (AMOS) Conference, Adelaide, South Australia, 5–8 Feb. [Available at http://eprints.usq.edu.au/1911/.]

Siedler, G., M. Rouault, and J. Lutjeharms (2006), Structure and origin of the subtropical South Indian Ocean Countercurrent, *Geophys. Res. Lett.*, *33*, L24609, doi:10.1029/2006GL027399.

Stramma, L. (1992), The South Indian-Ocean current, *J. Phys. Oceanogr.*, *22*(4), 421–430.

Stramma, L., and J. R. E. Lutjeharms (1997), The flow field of the subtropical gyre of the South Indian Oceans, *J. Geophys. Res.*, *102*(C3), 5513–5530, doi:10.1029/96JC03455.

Strang, G. (2007), *Computational Science and Engineering*, 1st ed., 725 pp., Wellesley-Cambridge Press, Wellesley, Mass.

Takeuchi, K. (1984), Numerical study of the subtropical front and the subtropical countercurrent, *J. Oceanogr. Soc. Jpn.*, *40*(5), 371–381, doi:10.1007/BF02303341.

Tippins, D., and M. Tomczak (2003), Meridional Turner angles and density compensation in the upper ocean, *Ocean Dyn.*, *53*, 332–342, doi:10.1007/s10236-003-0056-5.

Tsubouchi, T., T. Suga, and K. Hanawa (2010), Indian Ocean Subtropical Mode Water: Its water characteristics and spatial distributions, *Ocean Sci.*, *6*, 41–50, doi:10.5194/os-6-41-2010.

Vallis, G. K. (2006), *Atmospheric and Oceanic Fluid Dynamics*, 745 pp., Cambridge Univ. Press, Cambridge, U. K.

Vianna, M. L., and V. V. Menezes (2010), Mean mesoscale global ocean currents from geodetic pre-GOCE MDTs with a synthesis of the North Pacific circulation, *J. Geophys. Res.*, *115*, C02016, doi:10.1029/2009JC005494.